

**MARITIME TRANSPORTATION RESEARCH AND EDUCATION CENTER
TIER 1 UNIVERSITY TRANSPORTATION CENTER
U.S. DEPARTMENT OF TRANSPORTATION**



**Corrosion Tolerant Pre-Stressed CFRP Fatigue Retrofits for Improved
Waterway Lock Reliability**

July 1, 2016 to September 15, 2018

Prepared by:

**Christine Lozano
Maggie Langston
Gary S. Prinz, Ph.D., P.E. (Project PI)**

**Department of Civil Engineering,
University of Arkansas, Fayetteville,
4190 Bell Engineering Center,
Fayetteville AR, 72701**

September 2018

FINAL RESEARCH REPORT

Prepared for:

Maritime Transportation Research and Education Center

**University of Arkansas
4190 Bell Engineering Center
Fayetteville, AR 72701
479-575-6021**

ACKNOWLEDGEMENTS & REPORT DISCLAIMER

This report presents the results of a research project sponsored by Maritime Transportation Research & Education Center (MarTREC). We acknowledge the financial and material support provided by MarTREC, the in-kind steel specimen donations from W&W|AFCO Steel, as well as the assistance and encouragement of Dr. Guillermo Riveros from the US Army Corps of Engineers. The research was conducted in the Steel Structures Research Laboratory (SSRL) at the University of Arkansas. Laboratory staff and students instrumental in the completion of this work include: David Peachee, Diego Real and Mark Kuss.

This material is based on work supported by the U.S. Department of Transportation under Grant Award Number DTRT13-G-UTC50. The work was conducted through MarTREC at the University of Arkansas.

The contents of this report reflect the views of the authors, who are responsible for the facts and the accuracy of the information presented herein. This document is disseminated under the sponsorship of the U.S. Department of Transportation's University Transportation Centers Program, in the interest of information exchange. The U.S. Government assumes no liability for the contents or use thereof.

EXECUTIVE SUMMARY

Lock gates are an important part of the transportation infrastructure within the United States (US), having many economic, safety, and environmental benefits over rail and highway transportation systems. Unfortunately, many existing lock gates throughout the US have reached or exceeded their initial design life and require frequent repairs to remain in service. Unscheduled repairs often increase as gates age, having a local economic impact on freight transport which can create economic ripples throughout the nation. Fatigue and corrosion are key causes of unscheduled service interruptions, degrading lock gate components over time. Additionally, because lock gates are submerged during operation, crack detection prior to component failure can be difficult, and repair costs can be high.

This report presents an analytical and experimental investigation into fatigue damage within common lock gate geometries, and develops fatigue mitigation strategies capable of extending gate service-life. The goal of the research program is to identify critical fatigue regions and locally extend gate component fatigue life. Detailed finite element analyses are combined with fatigue and fracture mechanics theories to predict critical fatigue regions within common gate details and develop retrofit strategies for mitigating fatigue cracking. Full-scale experimental fatigue testing of a critical lock gate component is conducted to provide a baseline for evaluation of retrofit strategies. Retrofit strategies using carbon fiber reinforced polymer (CFRP) plates having optimized pre-stress levels are discussed.

TABLE OF CONTENTS

List of Figures	6
List of Tables	9
Notation	11
1. Introduction.....	13
1.1. Overview	13
2. Review of Relevant Literature.....	17
2.1. Fatigue in Steel Lock Gates and Review of Analysis Methods	17
2.2. Review of Fatigue Retrofit Methods.....	18
2.2.1. <i>Weld Surface Treatment</i>	18
2.2.2. <i>Hole-Drilling in Steel Sections</i>	18
2.2.3. <i>Vee-and-Weld</i>	18
2.2.4. <i>Doubler/Splice Plates</i>	19
2.2.5. <i>Post-Tensioning</i>	19
2.3. Overview of CFRP and Review Applications in Structural Retrofits.....	19
3. Analytical Investigation into Lock Gate Component Fatigue	21
3.1. Selection of Lock Gate for Analysis	21
3.2. Modeling Techniques.....	21
3.2.1. <i>Geometry and Boundary Conditions</i>	21
3.2.2. <i>Loading</i>	24
3.3. Determination of Fatigue Damage	25
3.3.1. <i>Miner's Total Damage</i>	26
3.3.2. <i>Cycle Counting</i>	26
3.4. Results and Discussion from Gate Analyses.....	26
3.4.1. <i>Fatigue Life Evaluation</i>	26
3.4.2. <i>Description of Detailed Fatigue Investigation for the Critical Component</i>	27
3.4.3. <i>Fatigue Endurance from Constant Life Diagrams: The Goodman Criterion</i>	28
3.4.4. <i>Required Pre-Stress for Fatigue Prevention using Goodman Constant Life Diagram</i>	30
3.4.5. <i>Effect of Pre-Stress on Component Fatigue Life</i>	31
3.4.6. <i>Revised Stress Calculations Following Retrofit Simulations</i>	32
3.4.7. <i>Pre-Stress Simulation Results</i>	33
4. Development of a Fatigue Retrofit Prototype	35
4.1. Investigation into Retrofit Bonding Strategies for Achieving Desired Pre-Stress Levels and Preventing Pre-Stress Losses	37

5. Experimental Investigation into Retrofit Fatigue Mitigation	41
5.1. Specimen Geometry	41
5.2. Loading	43
5.3. Experimental Setup and Testing Matrix	45
5.4. Instrumentation and Monitoring	46
5.5. Experimental Fatigue Test Results	47
5.5.1. Testing Observations from Full-Scale and Half-Scale Specimens	47
5.5.2. Effect of Retrofit Pre-Stress Levels on Specimen Local Stresses	49
5.5.3. Effect of Pre-Stressed Retrofit on Specimen Fatigue Life	50
5.5.4. Performance of Half-Scale Retrofit Clamping Mechanisms during Cyclic Loading	52
6. Summary and Conclusions.....	53
References	55
Appendix A1-A6.....	59-73

LIST OF FIGURES

Figure 1. Function of lock gates within the lock system. 1) The lower gate is lowered allowing entrance to the lock. 2) The lower gate closes and the water level changes. 3) The upper gate opens allowing the vessel access to the higher water elevation.....	13
Figure 2. Marine highway routes within the US [4].....	14
Figure 3. Transportation costs per ton (Port of Pittsburg, 2014).....	14
Figure 4. Cargo capacity equivalency	14
Figure 5. Elevation view of Greenup Lock and Dam geometry.....	16
Figure 6. Example of an un-bonded CFRP retrofit [18].....	16
Figure 7. Project task timeline	17
Figure 8. Stress flow and concentration around a hole (adapted from figure in [20])	17
Figure 9. Vee and weld fatigue repair method	19
Figure 10. Stress amplitude reduction (Doubler/Splice Plates) and Shifted Mean Stress (Post-Tensioning)	19
Figure 11. Section view diagram of CFRP.....	20
Figure 12. Bonded CFRP strips used to strengthen concrete structure [30].....	20
Figure 13. CFRP vs Steel elastic modulus.....	21
Figure 14. Upstream elevation and top view of a lock gate (Greenup Lock and Dam, Ohio River).....	22
Figure 15. Section through leaf and recess of Lock Gate #1 (Greenup Lock and Dam, Ohio River).....	22
Figure 16. Lock Gate #1: detail of diagonal connection	23
Figure 17. Lock Gate #1: section view of the quoin end.....	23
Figure 18. Lock Gate #1: section view of miter end	23
Figure 19. Lock Gate #1: upstream elevation diagram and applied boundary conditions for one Lock Gate leaf	24
Figure 20. Lock gate in empty lock.....	24

Figure 21. Different hydrostatic load levels applied on the gate (ft. – in.) and simulation of water level elevation change through hydrostatic load amplitude triggering.....	25
Figure 22. Greenup Lock and Dam von Misses Stress contour and numbered sections of high stress concentrations with stress graphs	25
Figure 23. von Misses Stress concentrations at the point of highest loading and the connection detail for the section	27
Figure 24. a) A submodel embedded in gate model with mesh view; b) 3-D of submodel with contours from loading applied to gate.....	28
Figure 25. Triangular (fillet) Weld geometry modeled as part of the solid element model.....	28
Figure 26. Components of cyclic stress	29
Figure 27. a) Unmodified Goodman diagram and yield line; b) Modified Goodman life diagram.	30
Figure 28. Modified Goodman Life Diagram with data point and stress shift	31
Figure 29. Free body diagram of the pre-stress force	31
Figure 30. Retrofit application on Section F13 in the FEA model	32
Figure 31. New Pre-stress force cross-section.....	33
Figure 32. Free body diagram used to calculate the pre-stress force.....	33
Figure 33. Stress range shift, in Section F13, due to applied CFRP pre-stress (1 lockage cycle).....	34
Figure 34. Goodman Life Diagram with stress shift change of Section F13 with the retrofit applying 35.2 kips pre-stress force	34
Figure 35. Retrofit components and assembly steps for the CFRP retrofit	36
Figure 36. Cross-section of pre-stress bearing mechanism with forces applied by bolts to create the pre-stress.....	36
Figure 37. Cross-section view of retrofit friction grip mechanism.....	37
Figure 38. Free body diagram of clamp, retrofit, and section 13 to determine the required friction force from known pre-stress force	37
Figure 39. Corroded (bottom) and uncorroded (top) steel surfaces.....	38
Figure 40. Static coefficient of friction test: a) static coefficient of friction free body diagram; b) test materials.....	38

Figure 41. Four bonding mechanisms for clamping the CFRP consisting of: (a) wedge grips, (b) sandpaper, (c) epoxy, and (d) Slipnot™ surface.....	39
Figure 42. Representation of CFRP stress data showing pre-stress loss due to bond failure.....	39
Figure 43. CFRP pre-stress measurements from the different bonding mechanisms considered.....	40
Figure 44. Measured CFRP pre-stress losses due to relaxation and creep.....	41
Figure 45. Measured temperature effects on CFRP pre-stress levels.....	41
Figure 46. Gate section F13 fabrication details for (a) full-scale specimen and (b) half-scale specimen.....	42
Figure 47. Notch location for (a) full-scale specimen and (b) half-scale specimen.....	42
Figure 48. Constant life diagram using the modified Goodman criteria for smooth and notched specimens.....	43
Figure 50. a) Stresses from submodel of Lock Gate; b) Stresses from model of test specimen.....	44
Figure 51. Experimental test setup and specimen force diagrams for (a) full-scale axially loaded specimen, (b) full-scale specimen in three-point bending, and (c) half-scale axially loaded specimen.....	45
Figure 53. Strain gage locations for the various specimen configurations: (a) full-scale axial, (b) full-scale 3-point, and (c) half-scale axial.....	47
Figure 54. Recorded strains, a) pre-notch; b) post-notch.....	48
Figure 55. Effect of CFRP pre-stressing on notch local stress history.....	49
Figure 56. Effect of CFRP pre-stress level on full-scale component stress state.....	50
Figure 57. Effect of CFRP pre-stress level on small-scale component stress state.....	50
Figure 58. Fatigue crack growth and eventual brittle fracture of specimen C3-3 following 989,235 cycles.....	51
Figure 59. Measured stress at the notch of specimen C3-3 (no retrofit) and specimen C3-4 (retrofit).....	51
Figure 60. Measured CFRP pre-stress during rapid cyclic loading.....	52

LIST OF TABLES

Table 1. List of gates on the Arkansas River System, completed date, and date of repair	15
Table 2. Types of CFRP based on modulus of elasticity and strength	20
Table 3. Fatigue damage calculations of critical sections	27
Table 4. AASHTO Life-Cycle Fatigue from model data	35
Table 5. Stresses from gate model of Greenup Lock & Dam gate 1 (35.2 kip Pre-Stress).....	35
Table 6. Test variations to confirm bond mechanism.....	40
Table 7. Coefficients for stress concentration factor [43]	43
Table 8. Experimental test matrix.....	46
Table 9. Experimental test matrix and resulting fatigue cycles applied	48
Table 10. Mean and amplitude stress shift due to CFRP pre-stress level.....	49
Table 11: List of identified critical sections, detail diagram, AASHTO category, and damage	59
Table 12. Parameters for Marin surface modification factor.....	65
Table 13: Reliability factors corresponding to 8% standard deviation of the endurance limit	67
Table 14: Calculated Marin modification factors summary and modified endurance limit	68

NOTATION

The following terms are used in the text of this report:

γ	=	fatigue load factor;
Δf	=	live load stress range due to the passage of the fatigue load;
ΔF_n	=	nominal fatigue resistance;
ΔF_{TH}	=	constant amplitude fatigue threshold;
A	=	detail category AASHTO Table 6.6.1.2.3-1 (ksi^3);
N	=	number of expected cycles to reach the nominal fatigue resistance;
D_i	=	total damage;
n_i	=	number of cycles;
N_i	=	number of cycles to failure;
$\Delta\sigma$	=	applied stress range;
S_e	=	fatigue endurance limit;
S'_e	=	estimated fatigue endurance limit;
k	=	modification factors in the Marin Equation;

RESEARCH REPORT

1. Introduction

1.1. Overview

Locks are essential for waterway transport along many river and canal systems, allowing passage of ships through regions of differing water elevation. Locks operate by creating a chamber of water that can be lowered or raised independently from the upstream or downstream elevations. Figure 1 shows a typical miter lock gate and the water elevation change process. As shown in Figure 1, two sets of gates open and close in sequence as the ship transitions to a higher water elevation.

The United States waterway transportation infrastructure is extensive, including over 12,000 miles of waterway (see Figure 2), and has economic, security, and environmental benefits over traditional rail or highway transport systems [1]. Other forms of transport such as rail or truck can be 5-10 times more expensive than waterway transport respectively (see Figure 3) [2]. As an example, barge transport along inland waterways of the upper Mississippi River generates a transportation cost savings of nearly \$1 billion dollars annually [3]. The most common type of barge used to transport goods along the major waterways is a 15-barge tow, which is equivalent to nearly 5 unit trains and 870 trucks (see Figure 4).

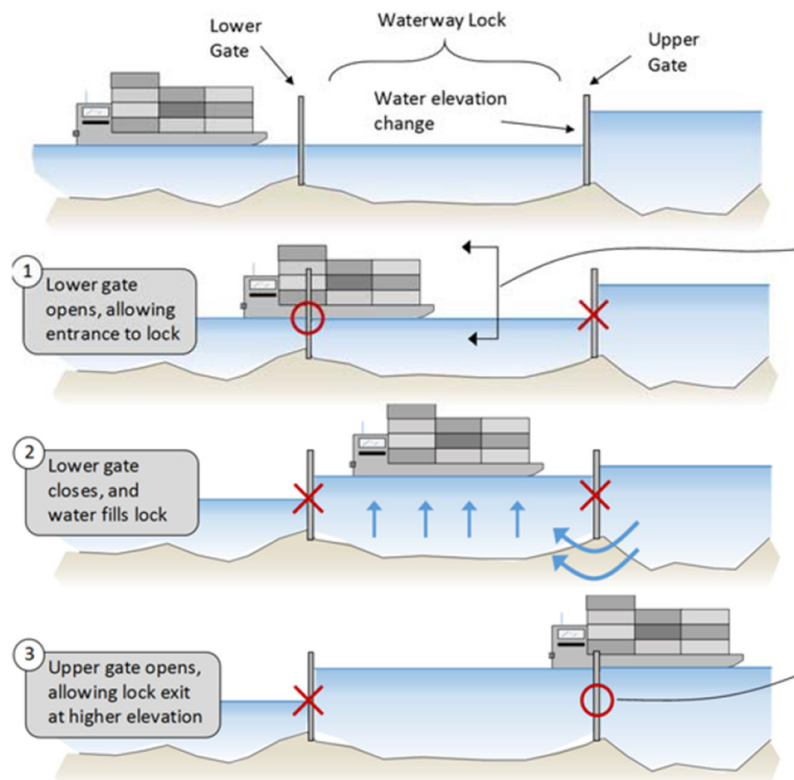


Figure 1. Function of lock gates within the lock system. 1) The lower gate is lowered allowing entrance to the lock. 2) The lower gate closes and the water level changes. 3) The upper gate opens allowing the vessel access to the higher water elevation.

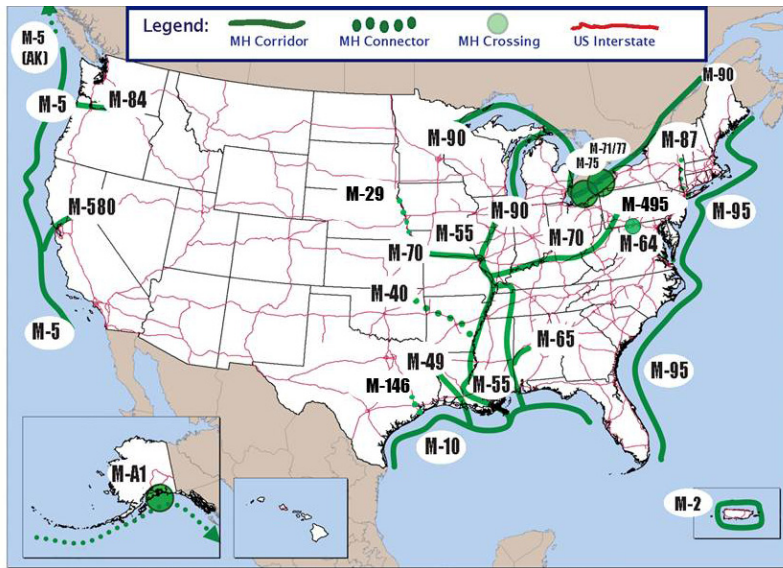


Figure 2. Marine highway routes within the US [4]

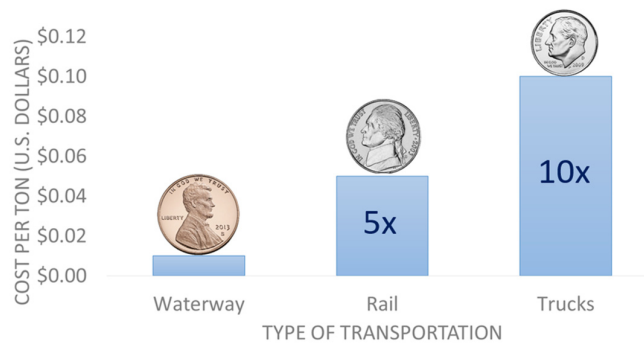


Figure 3. Transportation costs per ton [2]

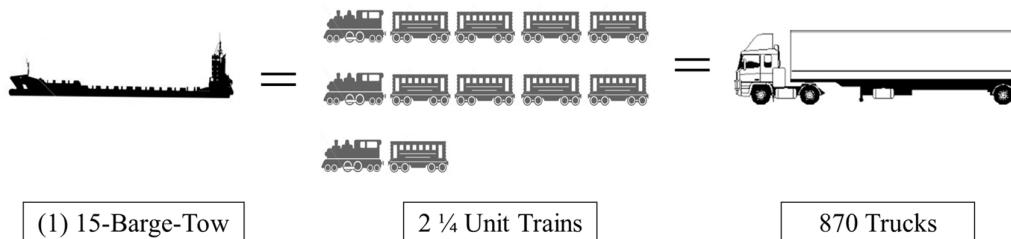


Figure 4. Cargo capacity equivalency

While locks are essential to waterway transport, many of the lock gates within the United States have reached or exceeded their design life. Many of the existing lock gates were designed for a service life of 50 years but have aged beyond this service-life expectancy, with additional locks getting older each year [5]. Some locks have even doubled their expected service life, having been constructed in the early 1900's. The Hiram M. Chittenden Locks in Seattle, Washington, turned 100 years old in 2017. As lock gates reach their design life, costly

repairs are often needed to maintain waterway access. Table 1 shows, the scheduled repairs for the locks on the Arkansas River System, with required repairs occurring after forty years of service (on average) [5].

Table 1. List of gates on the Arkansas River System, completed date, and date of repair

Lock/Dam	Started/Completed	Repairs	Years Before Repairs (yrs.)
Arthur V. Ormond Lock and Dam No. 9	1965/1969	N/A	N/A
Choteau Lock No. 17	1967/1970	2012	42
Dardanelle Lock and Dam No. 10	1957/1969	2017	48
David D. Terry Lock and Dam No. 6	1965/1968	2009	41
Emmett Sanders Lock and Dam No. 4	1964/1968	N/A	N/A
J. W. Trimble Lock and Dam No. 13	1965/1969	N/A	N/A
Joe Hardin Lock and Dam No. 3	1963/1968	2013	45
Lock and Dam No. 5	1964/1968	N/A	N/A
Montgomery Point Lock and Dam	1998/2004	2015	11
Murray Lock and Dam No. 7	1964/1969	2015	46
Newt Graham Lock No. 18	1967/1970	N/A	N/A
Norrell Lock and Dam No. 1	1963/1967	N/A	N/A
Norrell Lock No. 2	1963/1968	2013	45
Ozark-Jeta Taylor Lock and Dam No. 12	1964/1969	N/A	N/A
Robert S. Kerr Lock and Dam No. 15	1964/1970	N/A	N/A
Toad Suck Ferry Lock and Dam No. 8	1965/1969	Canceled	Canceled
W. D. Mayo Lock No. 14	1966/1970	2014	44
Webber Falls Lock and Dam No. 16	1965/1970	2016	46
Average age before repair			40

Unscheduled maintenance and repair of lock gates can be expensive and cause economic ripples throughout the entire inland waterway network. As an example, the 2002 upstream lock gate failure on the John Day Lock resulted in eight months of required repairs [6]. A gate deterioration failure within the Greenup Lock in 2003 resulted in an estimated \$14 million in losses to barge companies from lost operating costs [7]. The McApline Lock in 2004 is another example, with failure of critical structural members causing over 1,440 hours of tow delays even with a closure notice of 2 months [8]. Failure of the downstream gate on the Dalles Lock in 2009 resulted in two transportation companies temporarily laying off half of their workers [9]. An unscheduled extension of repairs on the Greenup Lock and Dam (which occurred during winter months) caused energy plants to ship coal by alternate means as stockpiles became depleted [7]. During these extended repairs on the Greenup Lock and Dam the MEMCO Barge Line company lost \$1.3 million [7]. The United States Army Corps of Engineers (USACE) states that waterway lock gates are the “most immediate critical infrastructure component” because of rapid degradation [10].

Fatigue and corrosion are key causes of lock gate component failures leading to unscheduled service interruptions. Fatigue damage occurs as structural components are subjected to frequently repeated loads, which in the case of a lock gate may include frequent water elevation changes or gate openings. Figure 5 shows a typical miter gate section and water elevation differences during normal operation. Specific parameters leading to fatigue damage include the applied component stress range (σ_a), applied mean stress (σ_m), as well as the aggressiveness of the structural environment. Typically, increases in stress range, mean stress, or the aggressiveness of the environment will lead to increased fatigue damage. Submerged water environments where lock gates are required to operate, promotes corrosion and unlike many other steel structures subjected to repeated loading, corrosion promoted fatigue does not have a fatigue limit, so failures are difficult to predict [11]. Fatigue tends to

occur first in connection details, especially those containing welds, due to locked-in residual stresses or geometry induced stress concentrations which shift locally the applied mean stress. Lock gates are primarily constructed of welded steel sections and many gates are at high risk for fatigue failures following years of service in a submerged corrosive environment.

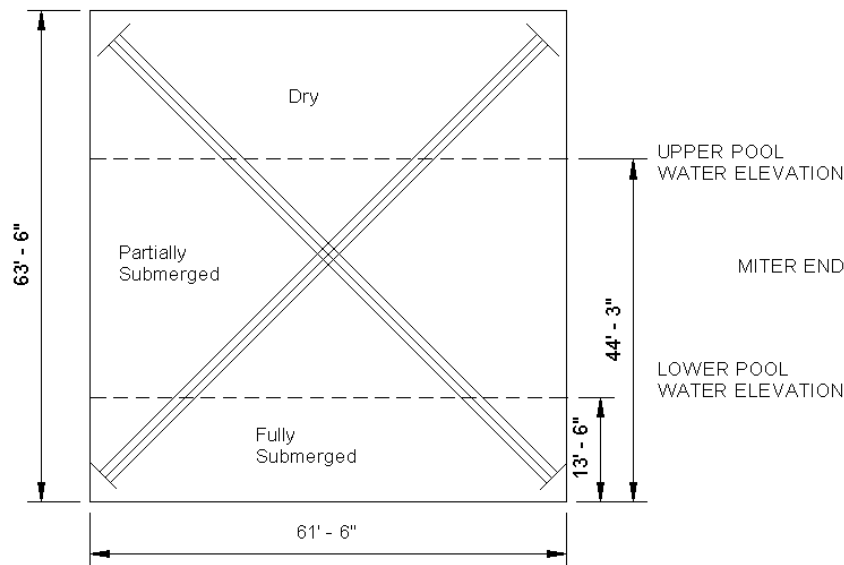


Figure 5. Elevation view of Greenup Lock and Dam geometry

Additionally, lock gates are partially submerged in water which can make it difficult to detect existing cracks. Because of this, existing cracks are often allowed to grow until failure disrupts normal gate service. Once a gate has experienced cracking and needs repair, the lock must be de-watered to allow access and favorable repair conditions.

The difficulty of crack detection and high repair costs have led to research on lock gate fatigue cracking and failures. Carbon fiber reinforced polymer (CFRP) materials have been used successfully as a crack mitigation method as they have a high strength to weight ratio, high resistance to environmental corrosion, and a high ease of onsite implementation [12, 13]. Additional CFRP research involving post-tensioned retrofits seems promising. Post-tensioned CFRP has been used in two different applications: 1) bonded to existing cracks, like a patch [14-16], and 2) in an un-bonded configuration [17-19] as seen in Figure 6.

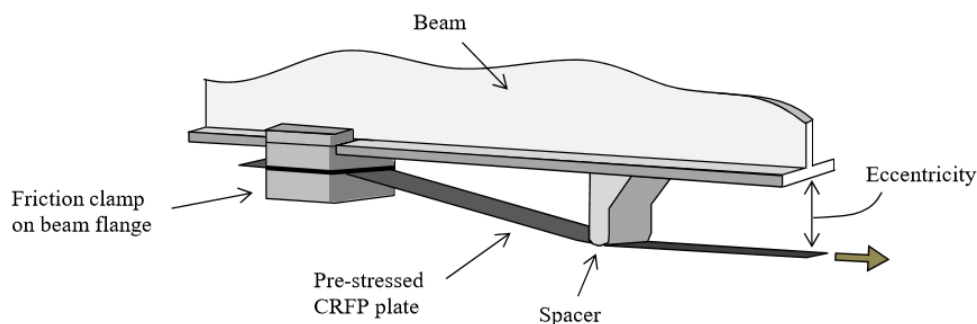


Figure 6. Example of an un-bonded CFRP retrofit [18]

This report presents an analytical and experimental investigation into fatigue damage within common lock gate geometries, and develops fatigue mitigation strategies capable of extending gate service-life. The goal of the research program is to identify the critical fatigue region and locally extend the lock-gate component fatigue life. Common lock gate geometries are identified with help from the US Army Corps of Engineers (project contact: Dr. Guillermo Riveros) and are analyzed using detailed finite element analyses. Stress data gathered from the analyses are used to inform novel pre-stressed fatigue retrofit strategies, and identify any retrofit geometry constraints. Corrosion-resistant CFRP material with potential application for the fatigue retrofits is investigated. Figure 7 shows the research project tasks, with Tasks 1 and 2 being presented in this report. Note that future research will involve field instrumentation of actual lock gate components which will inform on the long term performance of the developed fatigue retrofits under actual gate service conditions.

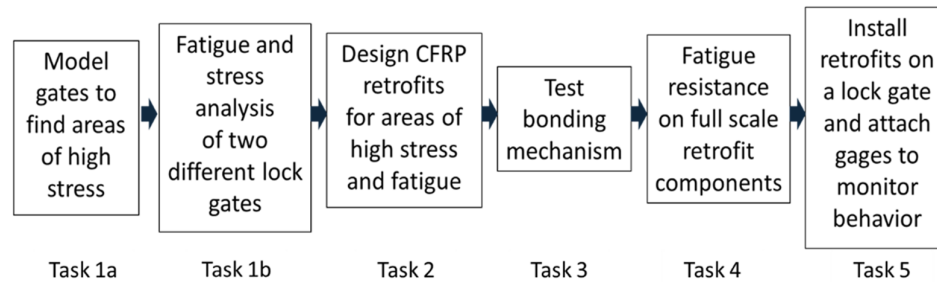


Figure 7. Project task timeline

2. Review of Relevant Literature

2.1. Fatigue in Steel Lock Gates and Review of Analysis Methods

Lock gates are prone to fatigue cracking due to the severity of the applied cyclic loads and aggressiveness of the corrosive environment. Connection regions where members are welded, bolted, and contain irregular geometric features often create stress concentrations that lead to high stress fluctuations and fatigue damage. Figure 8 shows how stress concentrations can develop, as the stresses “flow” around geometric features [20]. Welded sections also tend to be more susceptible to fatigue cracking as they introduce heat-induced flaws in the metal microstructure [21].

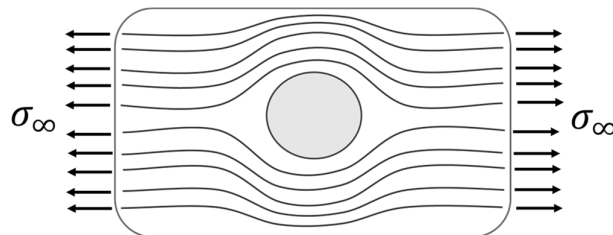


Figure 8. Stress flow and concentration around a hole (adapted from figure in [20])

While it can be difficult to account for local geometric features and their effects on local stress ranges, the American Association of State Highway Transportation Officials (AASHTO) has developed common component details and their corresponding fatigue capacities based on applied nominal stresses [22]. The detail categories (A, B, B', C, C', D, E, and E') found in

[22] are determined based largely on experimental testing of different component geometries. All fatigue detail capacities take the form of Equation 1:

$$(\Delta F)_n = (A/N)^{\frac{1}{3}} \quad \text{Equation 1}$$

where A is a constant representing the intercept of the stress versus number of cycles to failure (S-N) curve taken from AASHTO Table 6.6.1.2.5-1 based on the detail type; N is the number of expected cycles to reach the nominal fatigue resistance $((\Delta F)_n)$ [22].

2.2. Review of Fatigue Retrofit Methods

There are many different fatigue retrofit methods currently in use; however, all methods aim to do one of two things: 1) reduce the applied component stress range (often by stiffening or softening the section), or 2) reduce the applied component mean stress (often through an induced pre-stress). Common methods include weld surface treatments, hole-drilling, vee-and-weld, adding doubler/splice plates, and post-tensioning. The following sections give a review of each of these methods.

2.2.1. Weld Surface Treatment

Surface treatments improve un-cracked weld strength by reducing abrupt geometric changes or removing locked-in tensile residual stresses. Surface treatments include grinding, gas tungsten arc or plasma re-melting of the weld toe, and impact treatments. Surface treatments improve fatigue strength by improving the weld geometry and reducing stress concentrations, eliminating discontinuities where fatigue cracks may propagate, and reducing residual tensile stresses. After the surface treatment has been applied, the damaging effects of any prior loading cycles are removed, and the next greatest S-N curve can be used to predict the life of the section. Surface treatments only affect the weld toes [23].

2.2.2. Hole-Drilling in Steel Sections

Hole drilling is a common method for alleviating high stress concentrations at the tip of existing fatigue cracks. This method incorporates fatigue analysis fundamentals, by removing the sharp notch at the crack tip, stopping the propagation of the crack under Mode I loadings but less effective for mixed mode loading. The hole also lessens the stress concentration by shifting the stresses around the sides of the hole, see again Figure 8. The hole size must be large enough to contain the full crack tip with required hole sizes sometimes ranging between 2-4 inches [23]. The hole drilling method is a simple way of slowing down crack growth by re-directing the stress path.

2.2.3. Vee-and-Weld

The vee-and-weld method is often used in conjunction with other methods to reduce the actual stress range experienced by the original crack [23]. Once a crack has been found, the area around the crack length is removed in a “V” shape and then refilled with weld metal, see Figure 9. One drawback of this method is that the weld must be done by a certified welder, and significant care must be taken to produce a quality weld. Additionally, studies conducted on the vee-and-weld method concluded that the resulting repaired fatigue life is only as good as the original detail [23-25].

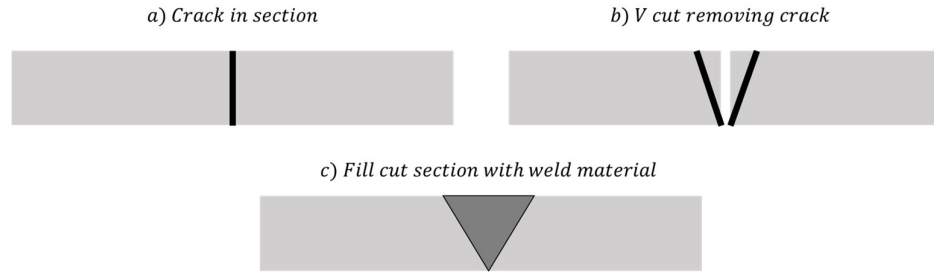


Figure 9. Vee and weld fatigue repair method

2.2.4. Doubler/Splice Plates

The addition of doubler or splice plates near fatigue prone details aim to reduce the applied stress range within the original component [26]. As the section area increases, the applied stress range is reduced (see Figure 10) and fatigue life is extended. One of the drawbacks of the doubler/splice plate method is the significant addition of weight to the structure.

2.2.5. Post-Tensioning

Fatigue cracks form by repeated stresses in tension causing a section to open and close. Post-tensioning considers the tensile stresses needed to create and propagate cracks by shifting the effective mean stress into a region of slight compression. Pre-stressed retrofits are placed on the section and introduce the tension required to shift the mean stress, see Figure 10. There are different methods to apply post-tension: pre-stressing strands, post-tensioning bars, or nuts torqued on high-strength rods. All the previously stated methods add tension to shift the effective mean stress partly or completely into compression [23].

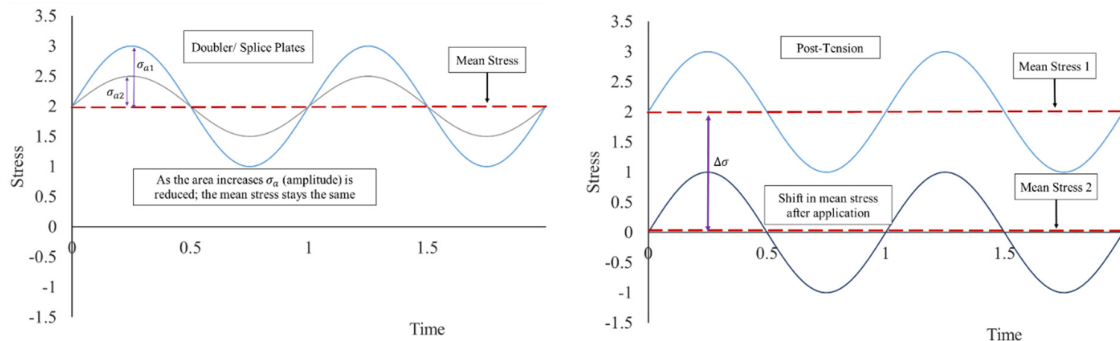


Figure 10. Stress amplitude reduction (Doubler/Splice Plates) and Shifted Mean Stress (Post-Tensioning)

2.3. Overview of CFRP and Review Applications in Structural Retrofits

CFRP is a composite material made of carbon fiber strands within a resin matrix. As seen in Figure 11, the carbon fiber strands are oriented laterally and longitudinally. The weave pattern allows CFRP to be flexible and moldable while still having significant strength in tension. Additionally, CFRP is corrosion resistant and has a high fatigue life. There are different types of CFRP with varying properties allowing for a broader use of the material. Table 2 gives a list of five of the most readily available types of CFRP. CFRP is currently used within different fields including the automotive, aerospace, sporting goods, and infrastructure

because of its strength, flexibility, corrosion resistance, high strength to weight ratio, and moldability.

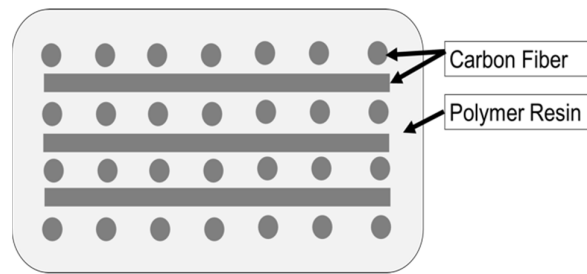


Figure 11. Section view diagram of CFRP

Table 2. Types of CFRP based on modulus of elasticity and strength

Type	Main Property
Ultra-High Modulus (UHM)	Modulus of Elasticity: >65,400 ksi
High Modulus (HM)	Modulus of Elasticity: 51,000-65,400 ksi
Intermediate Modulus (IM)	Modulus of Elasticity: 29,000-51,000 ksi
High Tensile, Low Modulus (HT)	Tensile Strength: >436 ksi Modulus of Elasticity: <14,500 ksi
Super High Tensile (SHT)	Tensile Strength: >650 ksi

Recently CFRP has been introduced as a strength and crack reduction retrofit in concrete and steel sections. CFRP has been used in concrete as a wrap-like retrofit to improve the tensile capacity of the section, see Figure 12. Current research has been conducted to determine the capacity of CFRP compared to steel and see how it works as a fatigue or strengthening retrofit [17, 27-29]. The elastic modulus of CFRP is similar to that of steel, but CFRP has a higher ultimate strength, see Figure 13. CFRP is less prone to corrosion than steel and has a lower weight to strength ratio (CFRP is about 20% of the mass of steel but with the same strength and elastic modulus [30]). Several studies have shown the advantages of using CFRP to increase flexural performance, by reinforcing tensile components, and extending fatigue life, by reducing the stress range or shifting the mean stress down [31-36].



Figure 12. Bonded CFRP strips used to strengthen concrete structure [30]

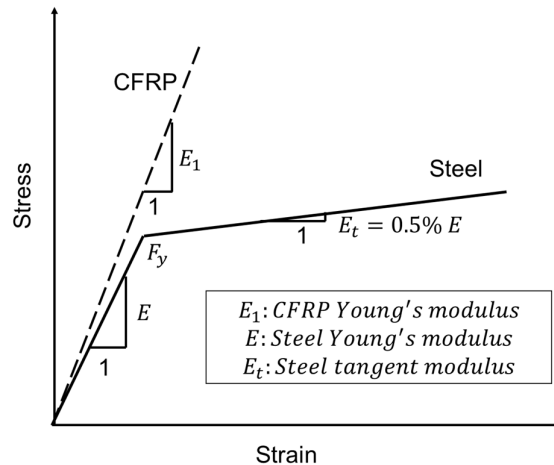


Figure 13. CFRP vs Steel elastic modulus

Pre-stressed CFRP has successfully been used, by [27, 28], to shift the mean stress in railroad bridges below the fatigue endurance limit increasing fatigue life. Research has proven that pre-stressed CFRP has increased the fatigue life of a steel section by up to 20 times [35, 37] with the thickness and pre-stress level of the CFRP being two important factors that influence how the retrofit performs. The current research aims to develop CFRP retrofits to reinforce critical fatigue details on lock gates.

3. Analytical Investigation into Lock Gate Component Fatigue

3.1. Selection of Lock Gate for Analysis

The selection of lock gates for analysis in this thesis were conducted with the assistance of the Army Corps of Engineers; the Corps oversees 239 lock systems throughout the United States. All lock gates considered are in-service, and in difficult environments to study without dewatering. The gate selection for this research project was based on maintenance and dewatering schedules of existing gates in conjunction with the project timeline. One gate selected for this project was the Greenup Lock and Dam on the Ohio River.

3.2. Modeling Techniques

3.2.1. Geometry and Boundary Conditions

A detailed finite element model considering local geometric features was created from construction documents obtained for the Greenup Lock and Dam on the Ohio River. All boundary conditions considered represent the operation of the constructed gate. The gate was modeled using the commercial finite element software ABAQUS [38]. Only one side of the lock gate was modeled due to symmetry. The dimensions of the gate are 63.5 feet by 61.5 feet by 5.71 feet, see Figure 14 and Figure 15. The gate was constructed from Grade 50 steel sections welded together. The gate diagonals (constructed from pre-tensioned rods) were simulated using linear spring elements pre-stressed to 22.9 ksi following the gate construction documents.

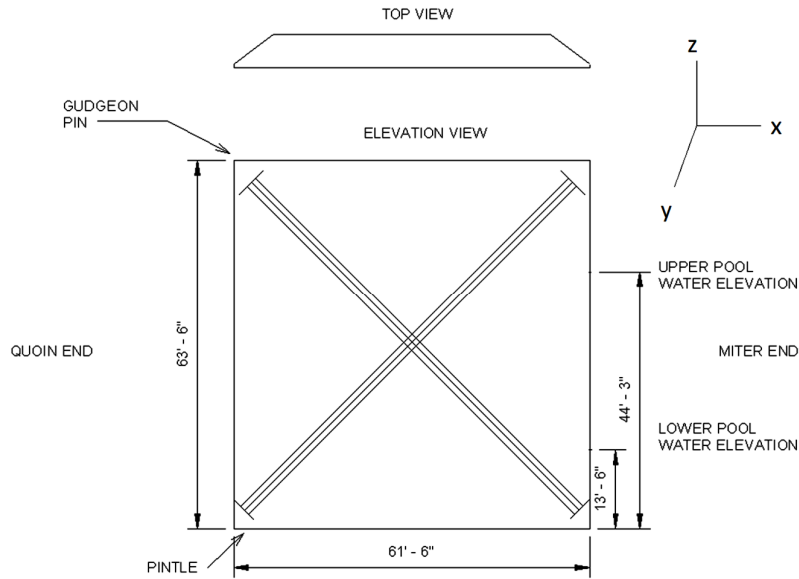


Figure 14. Upstream elevation and top view of a lock gate (Greenup Lock and Dam, Ohio River)

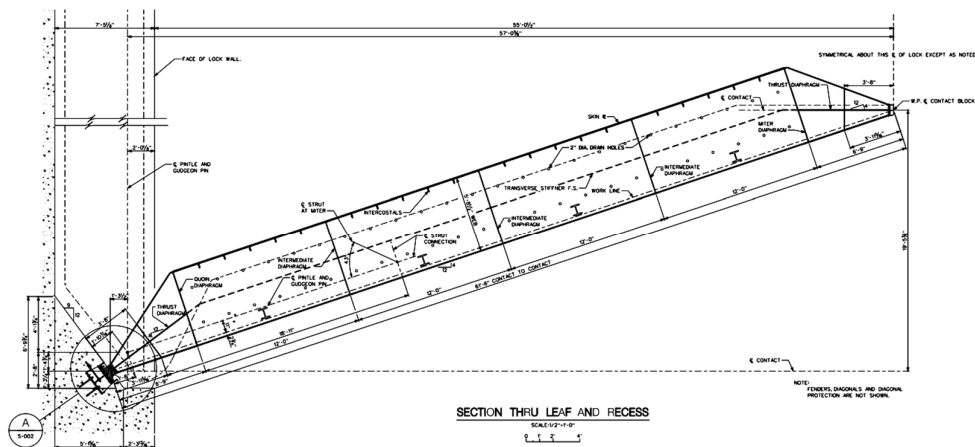


Figure 15. Section through leaf and recess of Lock Gate #1 (Greenup Lock and Dam, Ohio River)

Shell elements were used to simulate the gate geometric features. A general mesh size of 2.5 inches was used throughout, balancing computation expense and stress accuracy near geometric features having high stress gradients. In locations where the diagonal spring elements connect to the gate structure, nodes were tied to create rigid body regions simulating the details seen in Figure 16, and avoid local stress concentrations at the spring gate attachment. At the gudgeon pin and pintle (see again Figure 14) nodes were tied to create rigid bodies to simulate the quoin blocks that are the point of rotation (shown in construction details of Figure 17 and Figure 18).

Boundary conditions chosen followed previous analyses performed by [39]. The boundary conditions were added to the following sections: the gudgeon pin was restrained in the X and Y directions as shown in Figure 19; the quoin and lock ends were restrained in the Y and Z directions; and the pintle was restrained in the X, Y, Z, XR (rotation about X), and YR, see

Figure 19. The boundary conditions on the quoin and miter ends were applied along the full length of the gate. The quoin and miter end boundary conditions restrict movement in the X and Y directions simulating the concrete dam on the quoin end and the other lock gate leaf on the miter end, see Figure 19 and Figure 20.

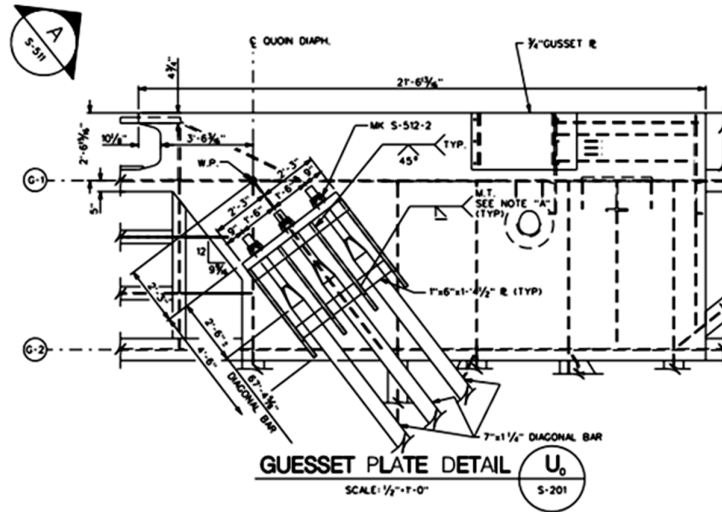


Figure 16. Lock Gate #1: detail of diagonal connection

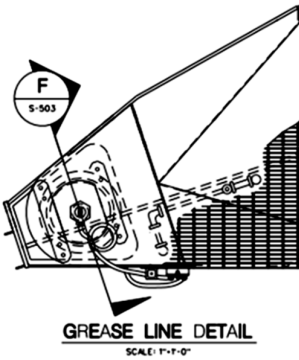


Figure 17. Lock Gate #1: section view of the quoin end

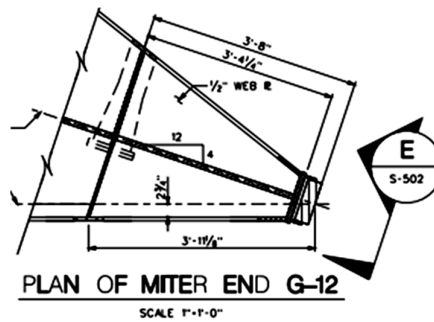


Figure 18. Lock Gate #1: section view of miter end

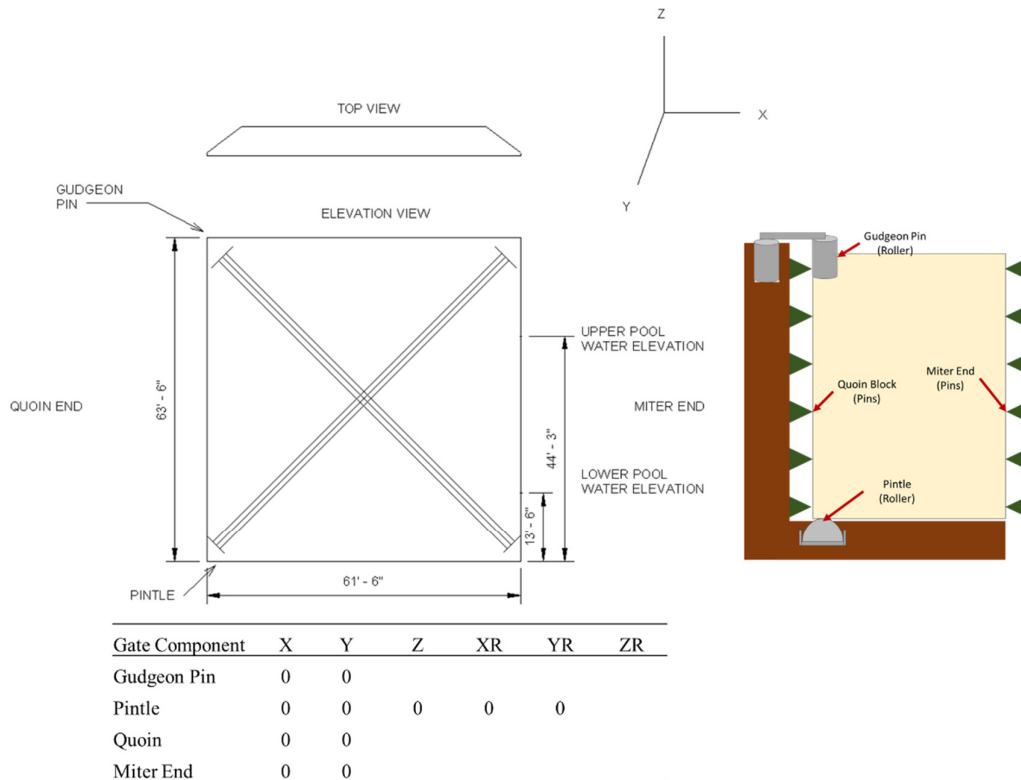


Figure 19. Lock Gate #1: upstream elevation diagram and applied boundary conditions for one Lock Gate leaf

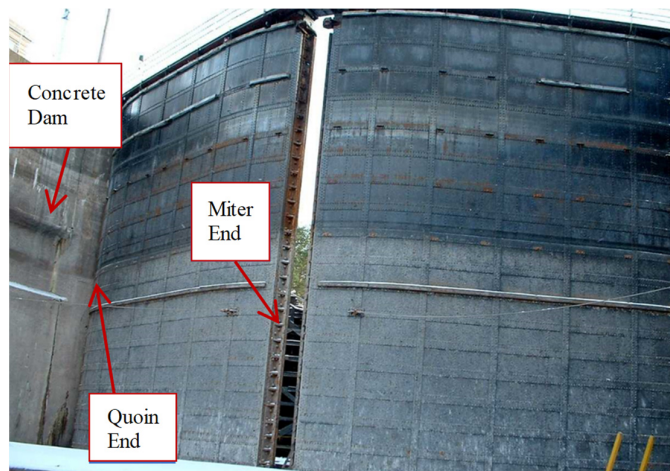


Figure 20. Lock gate in empty lock

3.2.2. Loading

All gate analyses consider gravity and hydrostatic loading. Changing water levels during lock operation are modeled using hydrostatic loads applied in sequential amplitudes to simulate a continuous rising water elevation. The load on the downstream face was set at the highest water level and remained constant during the analyses (see Figure 21). In Figure 21 the varying hydrostatic pressures applied to the upstream face are illustrated as a sequence of

applied triangular ramping loads which provide a constantly increasing hydrostatic pressure corresponding to the increasing water level. The various load amplitudes turn one load on and off at different analysis “steps”; however, the magnitude of any two amplitudes always adds to one, allowing smooth transition from elevation to elevation.

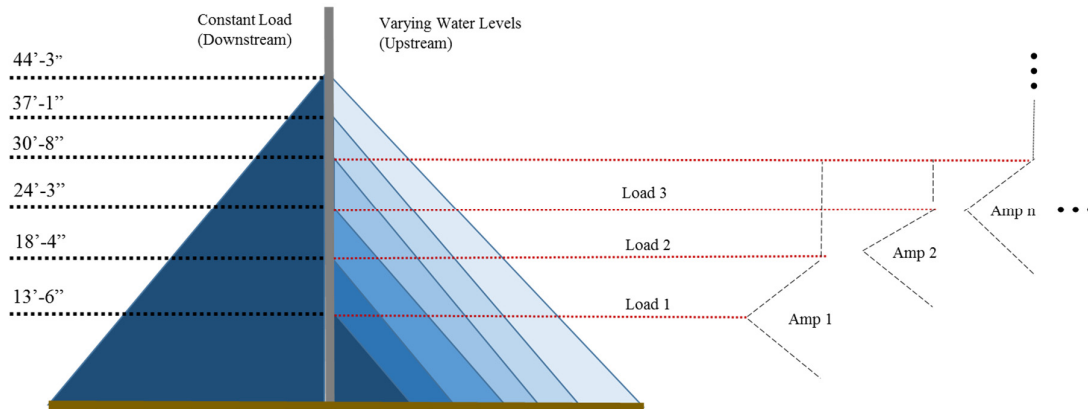


Figure 21. Different hydrostatic load levels applied on the gate (ft. – in.) and simulation of water level elevation change through hydrostatic load amplitude triggering

3.3. Determination of Fatigue Damage

The purpose of the gate model is to determine regions of high fatigue susceptibility. This is achieved by first identifying regions of high local stress fluctuation. As seen in Figure 22, high-stress regions can be determined from stress contours. The regions of high stress are compared to the AASHTO fatigue categories considering nominal applied stress ranges. Twenty-seven sections were determined to have high-stress concentrations. These sections are presented in Appendix A1.

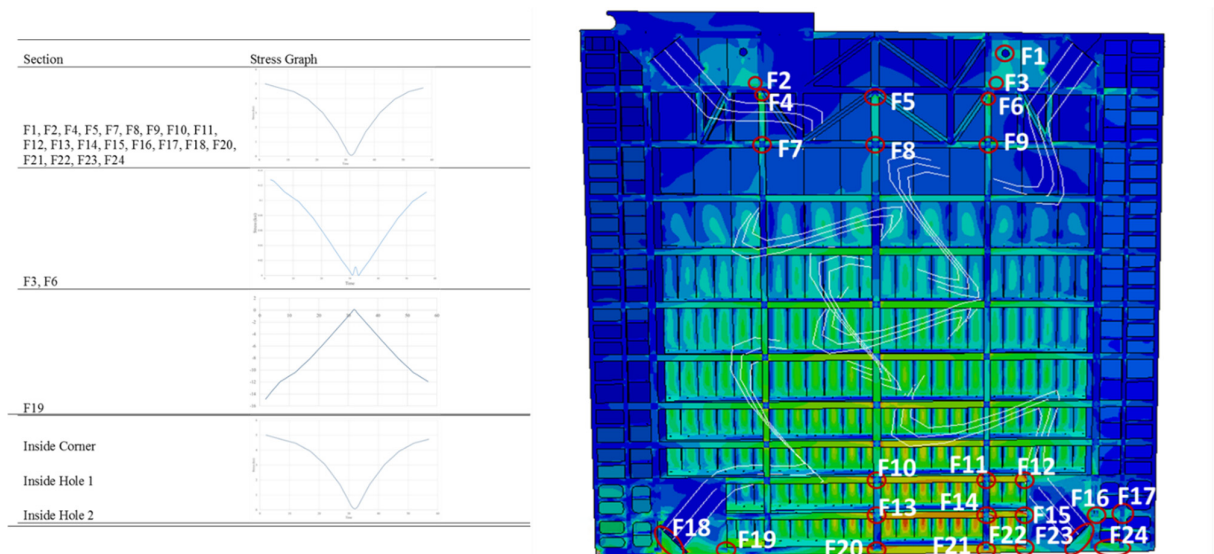


Figure 22. Greenup Lock and Dam von Mises Stress contour and numbered sections of high stress concentrations with stress graphs

3.3.1. Miner's Total Damage

The damage caused by one water elevation-change cycle for each gate component was determined using Miner's linear damage accumulation rule (referred hereafter as Miner's rule). When using Miner's rule, higher stress ranges cause greater fatigue damage. Miner's rule is presented in Equation 2:

$$\sum D_i = \sum \frac{n_i}{N_i} \quad \text{Equation 2}$$

where D_i is the total damage, n_i is the number of cycles, and N_i is the number of cycles to failure. N_i can be calculated from the AASHTO fatigue capacity equation, here re-arranged as Equation 3:

$$N_i = A * (\Delta\sigma)^{-3} \quad \text{Equation 3}$$

where A is the detail category acquired from AASHTO Table 6.6.1.2.3-1, and $\Delta\sigma$ is the applied stress range (determined from the finite element simulations).

3.3.2. Cycle Counting

In order to evaluate fatigue damage using Equations 2 and 3, stress cycle counts and corresponding stress ranges from the analyses must be known. Two common methods of cycle counting are the rain-flow counting method and the reservoir method (see Appendix A2 for details on each method). Based on the graphs generated from the stress-time data (shown in Figure 22), the reservoir method was chosen and the amount of damage per section was calculated using Miner's Rule.

3.4. Results and Discussion from Gate Analyses

The fatigue analyses conducted for this research use the stress based method provided by AASHTO and Miner's linear damage accumulation rule. Note that the AASHTO stress based method has been used successfully to design fatigue prone bridge components.

3.4.1. Fatigue Life Evaluation

Table 3 presents the accumulated fatigue damage during water-elevation change throughout the various gate components. From Table 3, and based on the applied stress range and detail category, Section F13 of Figure 22 accumulates the most fatigue damage during one water-elevation change cycle. Figure 23 shows the von Mises stress concentrations within the gate (at the stage of largest water elevation difference) along with the welded connection detail for the area with the highest fatigue damage.

Section F13 was similar in detail to sections F7-F11, F13-F14, and F20. These sections were all characterized as having the same detail category, AASHTO detail category E, but Section F13 was identified as the area of highest fatigue damage due to a high-stress concentration coupled with a small cross-sectional area when compared to the other detail sections on the gate. Section F13 is also situated in the middle near the bottom of the gate where the hydrostatic pressure difference is the greatest. Section F13 also has a smaller cross-sectional area than section F20 (the point of highest hydrostatic pressure).

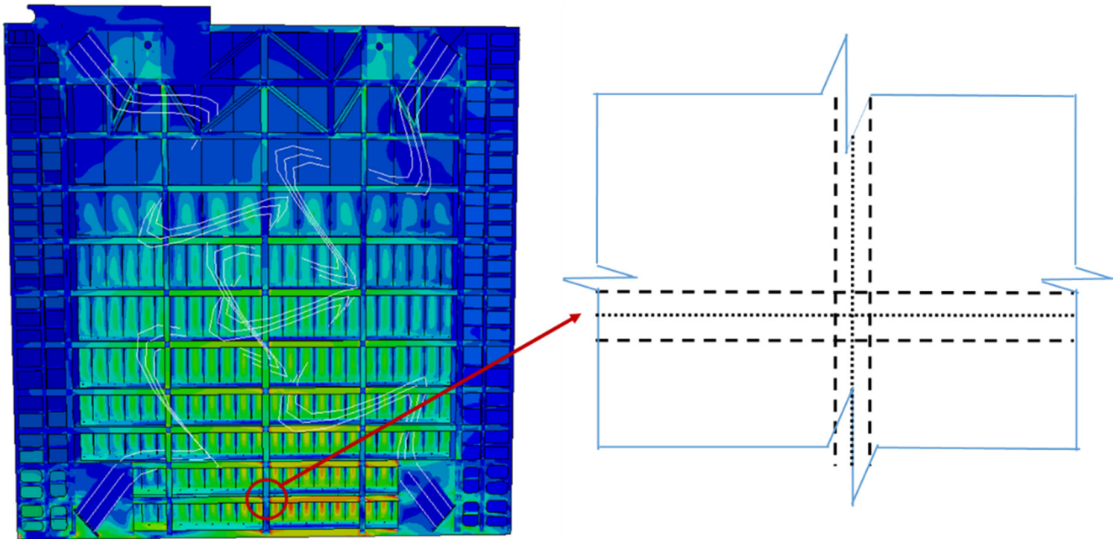


Figure 23. von Misses Stress concentrations at the point of highest loading and the connection detail for the section

Table 3. Fatigue damage calculations of critical sections

Location	Category	Type	No. Cycles	$\Delta\sigma$	A (ksi ³)	Δf (ksi)	Nf (cycles)	Damage (N/Nf)	Total Damage Per Section
Section F7	E	7.1	1	5.945	1.10E+09	4.5	5.235E+06	1.910E-07	1.910E-07
Section F9	E	7.1	1	7.093	1.10E+09	4.5	3.082E+06	3.244E-07	3.244E-07
Section F10	E	7.1	1	22.732	1.10E+09	4.5	9.364E+04	1.068E-05	1.068E-05
Section F11	E	7.1	1	22.52	1.10E+09	4.5	9.631E+04	1.038E-05	1.038E-05
Section F12	E	7.1	1	21.584	1.10E+09	4.5	1.094E+05	9.141E-06	9.141E-06
Section F13	E	7.1	1	23.444	1.10E+09	4.5	8.537E+04	1.171E-05	1.171E-05
Section F14	E	7.1	1	23.301	1.10E+09	4.5	8.695E+04	1.150E-05	1.150E-05
Section F15	E	7.1	1	22.022	1.10E+09	4.5	1.030E+05	9.709E-06	9.709E-06
Section F16	E	7.1	1	9.807	1.10E+09	4.5	1.166E+06	8.574E-07	8.574E-07
Section F17	E	7.1	1	9.807	1.10E+09	4.5	1.166E+06	8.574E-07	8.574E-07
Section F20	E	7.1	1	22.411	1.10E+09	4.5	9.773E+04	1.023E-05	1.023E-05
Section F21	E	7.1	1	21.916	1.10E+09	4.5	1.045E+05	9.570E-06	9.570E-06
Section F22	E	7.1	1	19.854	1.10E+09	4.5	1.406E+05	7.114E-06	7.114E-06
Section Inside 1	D	1.5	1	12.534	2.20E+09	7	1.117E+06	8.950E-07	8.950E-07
Section Inside 2	D	1.5	1	10.37	2.20E+09	7	1.973E+06	5.069E-07	5.069E-07

3.4.2. Description of Detailed Fatigue Investigation for the Critical Component

While the nominal stress based approach in AASHTO is useful for comparing the propensity for fracture between various details, more detailed fatigue investigations are useful for understanding the underlying fatigue causes and identifying strategies for damage prevention. For this purpose, a submodel of Section F13 is created to acquire more refined stress data from solid element types (ABAQUS element type C3D8R) within the specific section. The submodel boundary conditions are informed from the main gate model deformations such that compatibility is ensured and the submodel represents the same loading as provided for the entire gate model. Figure 24a) shows the Section F13 submodel integrated with the larger gate model while Figure 24b) shows the submodel without the gate. In addition to the refined stress data, the submodel allows simulation of weld geometry effects within the component that are

impractical to include in the larger-scale gate simulations. For the submodel, section welds are modeled as triangular fillet welds, within the same submodel part, corresponding to the construction documents provided (see Figure 25).

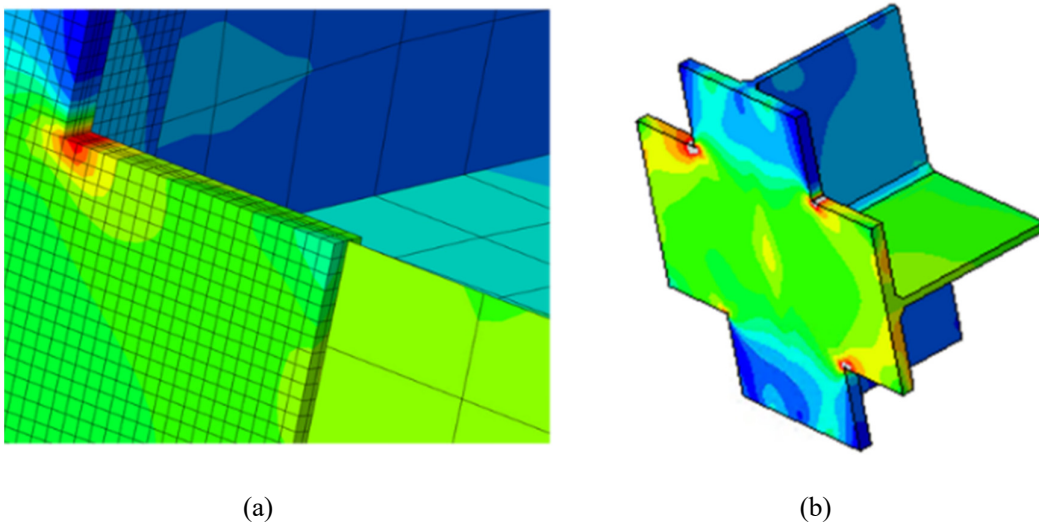


Figure 24. a) A submodel embedded in gate model with mesh view; b) 3-D of submodel with contours from loading applied to gate

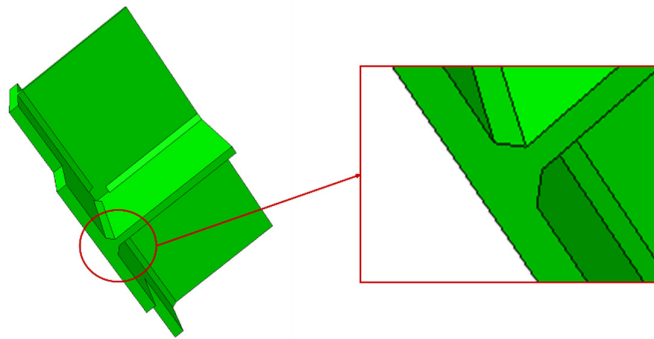


Figure 25. Triangular (fillet) Weld geometry modeled as part of the solid element model

In addition to local geometric features, the submodel considers a more refined mesh of 0.25in for capturing detailed stress information within regions having high stress gradients. Note that the main gate model had a mesh size equal to 2.5in.

A mesh convergence study helped determine the appropriate mesh size for the submodel used in this study, balancing computational expense and accuracy. In the mesh convergence study, mesh sizes at 0.25in, 0.13in, and 0.1in resulted in similar stresses (less than 0.3% difference) near the component corner (see again Figure 24(b)) indicating that the considered 0.25in mesh fully captures the stress gradient present in the component detail.

3.4.3. Fatigue Endurance from Constant Life Diagrams: The Goodman Criterion

Different from the nominal stress analysis using the AASHTO detail categories, local stress-states within the gate component (as informed by the submodel) can help determine fatigue

damage from interacting mean stresses and stress ranges. This information is helpful in identifying strategies for fatigue mitigation within local component regions. Constant life diagrams provide the mean stress and stress range interactions for determining the fatigue endurance limit, with the Goodman criterion (see Equation 4) being commonly used for low carbon structural steels. In Equation 4, S_e is the fatigue endurance limit (having zero mean stress), S_{ult} is the material ultimate strength, and σ_a and σ_m are the stress range and mean stress as provided in Equation 4 and Equation 5 respectively.

$$\frac{\sigma_a}{S_e} + \frac{\sigma_m}{S_{ult}} \leq 1 \quad \text{Equation 4}$$

$$\sigma_m = \frac{\sigma_{max} + \sigma_{min}}{2} \quad \text{Equation 5}$$

$$\sigma_a = \sigma_{max} - \sigma_{min} \quad \text{Equation 6}$$

In Equations 5 and 6, σ_{max} is the maximum stress while σ_{min} is the minimum stress, experienced during the loading cycles. The fatigue endurance limit (S_e) was determined using the Marin equation, shown in Equation 7 [40].

$$S_e = k_a k_b k_c k_d k_f S'_e \quad \text{Equation 7}$$

where the modification factors $k_a, k_b, k_c, k_d,$ and k_f are respectively based on surface condition, size, load, temperature, reliability, and miscellaneous effects. S'_e is estimated using Equation 8 given by [41].

$$S'_e = \begin{cases} 0.5 * S_{ult} & S_{ult} \leq 200 \text{ ksi} \\ 100 \text{ ksi} & S_{ult} > 200 \text{ ksi} \end{cases} \quad \text{Equation 8}$$

The calculated fatigue endurance limit for the lock gate components in this study is $S_e = 18.8 \text{ ksi}$. The detailed procedure used to determine S_e and the modification factors is provided in Appendix C.

For graphical reference, Figure 26 shows the various stress components used in the Goodman criterion and Figure 27 shows an example Goodman constant life diagram bound the yield stress, referred to as a “modified” Goodman diagram. In Figure 27, the yield stress bound prevents fatigue infinite life determination under high plasticity, as different fracture mechanisms participate in the damage. Note also in Figure 27, that $\sigma_m - \sigma_a$ combinations that fall underneath the modified Goodman diagram line result in an infinite fatigue life, prior to corrosion effects.

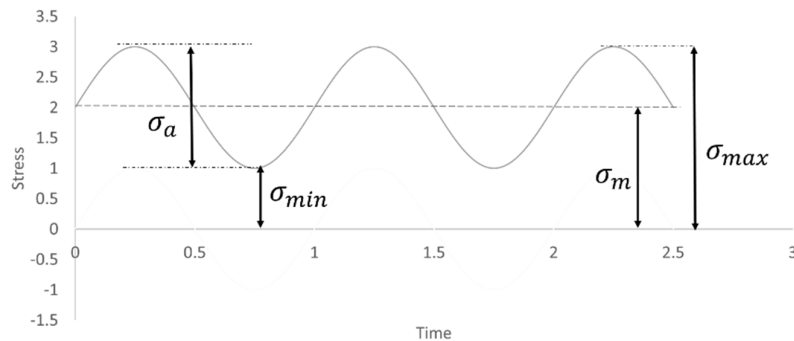


Figure 26. Components of cyclic stress

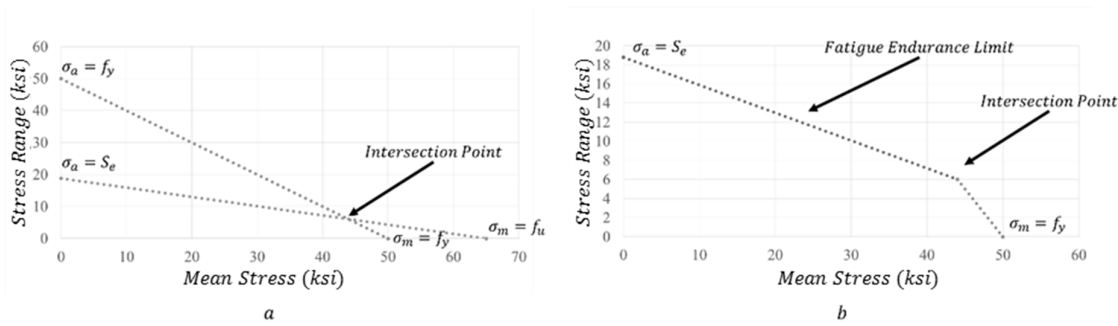


Figure 27. a) Unmodified Goodman diagram and yield line; b) Modified Goodman life diagram.

This study uses a modified Goodman diagram for determining the fatigue endurance limit of the lock gate component which is useful for determining what changes to the stress state are needed to improve the fatigue performance.

3.4.4. Required Pre-Stress for Fatigue Prevention using Goodman Constant Life Diagram

Figure 28 shows the Goodman life diagram created using the data from the submodel and $S_e = 18.8 \text{ ksi}$. The max principal stress data from the submodel is analyzed to determine a max amplitude and mean stress using Equations 5 and 6. Section F13 has a maximum mean stress of 22.32 ksi and a maximum stress range amplitude of 21.58 ksi resulting in a finite fatigue life (as expected) as shown on the diagram (note in Figure 28 the values fall outside the Goodman line). The stress data from the submodel corresponds to one water change cycle (lockage); however, the Lockages are repeated thousands of times throughout a year, and over a period of 50 years (the design life of the gate), the amount of cycles the section experiences outside of the fatigue endurance limit can lead to cracking.

This Goodman diagram is useful in determining the required mean stress shift such that the component falls within the Goodman line and experiences infinite fatigue life, regardless of past damaging cycles. The retrofit strategy taken herein considers an external applied pre-stress such that the mean stress shift transitions the stress state to the edge of the endurance limit. The total amount of pre-stress needed for this can be found by calculating the σ_m change needed on the Goodman diagram. As the mean stress shifts the amplitude of the stress range also decreases as 40% of the compressive stress cycles are not considered in the fatigue evaluation [42]. Figure 28 shows the shift in the mean stress along with the reduction of amplitude which is presented in Equation 9.

$$\sigma_{af} = \frac{\sigma_{max} - (\sigma_{mo} - \sigma_m) - ((\sigma_{min} + 1) - (\sigma_{mo} - \sigma_m)) * 60\%}{2} \quad \text{Equation 9}$$

In Equation 9, σ_{max} is the maximum principle stress from the submodel analysis, σ_{mo} is the initial mean stress, σ_{min} is the minimum principle stress from the submodel analysis, σ_m is the new mean stress, and σ_{af} is the newly calculated amplitude stress. The change in mean stress, $\Delta\sigma_m$, for gate Section F13 (based on the submodel analysis) is calculated to be 18.78ksi (which is rather large).

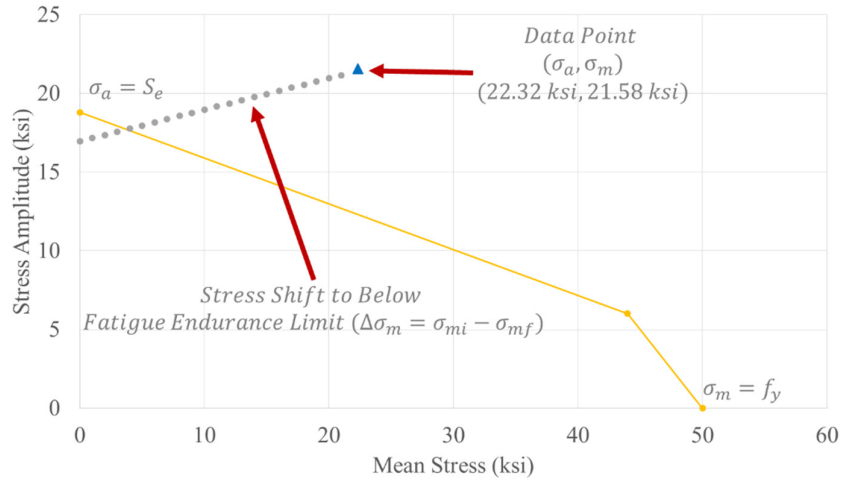


Figure 28. Modified Goodman Life Diagram with data point and stress shift

The required tension force to shift the mean stress by 18.78ksi can be found from the geometry of section and pre-stress application strategy. A free body diagram of the pre-stress retrofit configuration considered is shown in Figure 29. In Figure 29, steel plates clamp to the gate section and a pre-stressing force applied at an eccentricity (e) from the gate section. Equation 10 calculates the pre-stress force, based on the resulting section stress, pre-stress force, applied moment (from the eccentricity), and section area.

$$F_{prestress} = \frac{\Delta\sigma_m}{\left(\frac{e \cdot t_p}{2 \cdot I}\right) + \left(\frac{1}{A}\right)} \quad \text{Equation 10}$$

In Equation 10, $F_{prestress}$ is the pre-stress force, $\Delta\sigma_m$ is the change in stress, e is the moment arm, t_p is the thickness of the gate component, I is the moment of inertia, and A is the area of the plate. The pre-stress force is $F_{prestress} = 8.8 \text{ kips}$. The pre-stress force is applied to the CFRP to shift the mean stress.

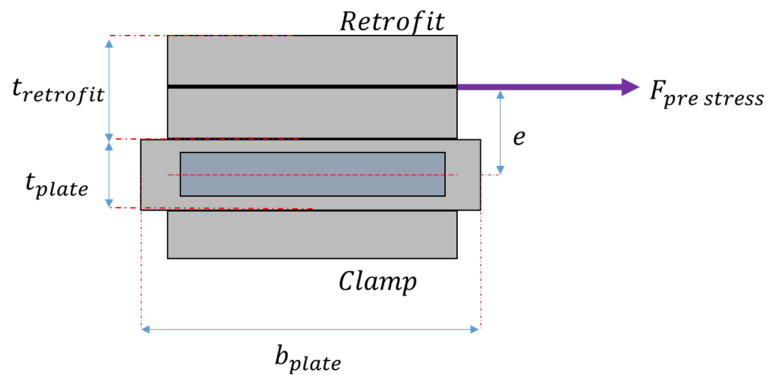


Figure 29. Free body diagram of the pre-stress force

3.4.5. Effect of Pre-Stress on Component Fatigue Life

To evaluate the effectiveness of the developed retrofit prestress, the designed pre-stress level of 8.8 kips is applied to the critical gate component (Section F13) in the full gate finite element simulation. Figure 30 shows the application method for the pre-stress, involving nonlinear springs and rigid body connection regions (simulating plate attachments). Stiffness of the nonlinear springs considers high modulus CFRP ($E = 51,000 \text{ ksi}$). Also shown in Figure 30, the simulated pre-stress is applied in the horizontal and vertical directions at section F13. In the simulation, the double configuration was chosen to counteract the multi-axial stresses induced by the hydrostatic pressure difference on either side of the gate. Note that the nonlinear springs are arbitrarily attached to the gate section $16\frac{3}{8} \text{ in.}$ from the component corners that experience the high stress concentration.

Resulting stress states within gate component indicate a slight reduction in mean stress; however, the shift was lower than predicted by the Goodman diagram and the component remained within the finite life region. This result indicates that higher pre-stress values are needed for significant fatigue life improvement and suggests a revision is needed to the pre-stress force calculation.

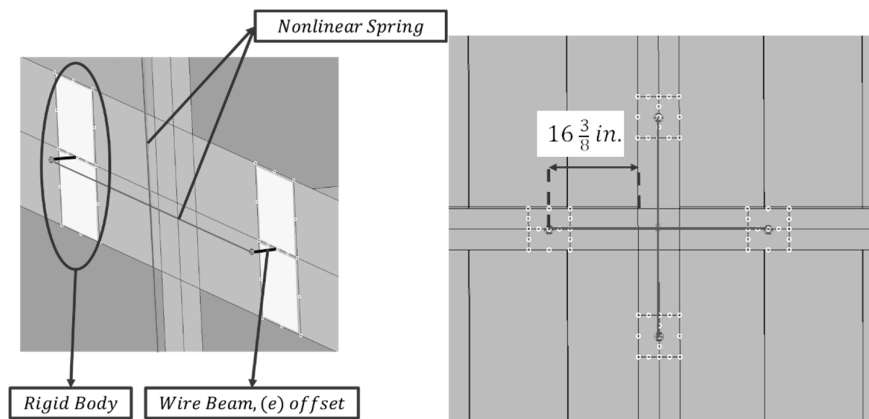


Figure 30. Retrofit application on Section F13 in the FEA model

3.4.6. Revised Stress Calculations Following Retrofit Simulations

The pre-stress calculations from Section 6 were based on stress shifts within a flat steel plate; however, the geometry of the gate sections differ greatly from this assumption. A revised calculation is needed that considers the entire Section F13 cross section as seen in Figure 31 and Figure 32. From the section stresses created from the free body diagram shown in Figure 32, the new cross-section requires a larger pre-stress force of 366.6 kips (nearly 42 times greater than previously predicted). Note that this pre-stress level is required for infinite life; however, given the large force required, increases to the finite life within the critical component may be more practical.

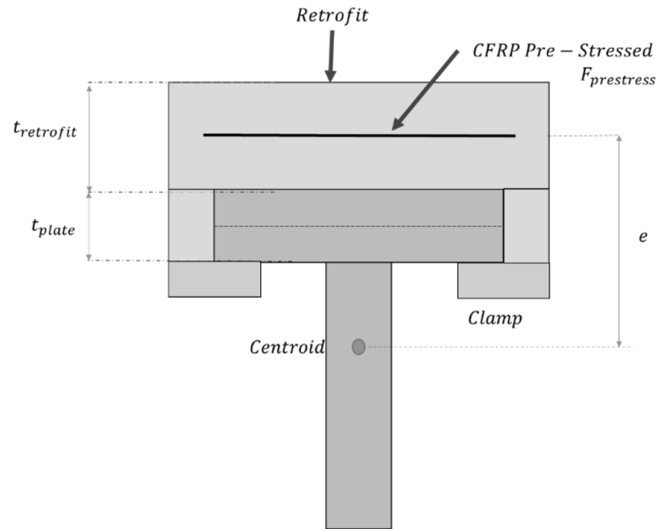


Figure 31. New Pre-stress force cross-section

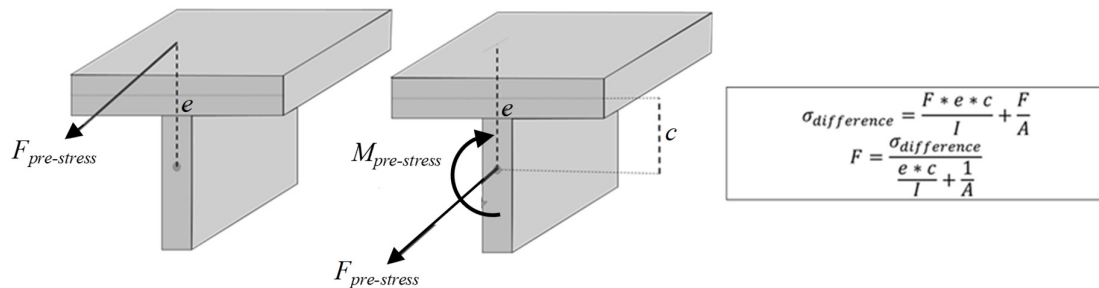


Figure 32. Free body diagram used to calculate the pre-stress force

As the required pre-stress force changes, the required friction force also changes due to the increased required pre-stress force. The greater pre-stress force creates a greater normal force, $N = 540$ kips, see Appendix E for calculations. The increased normal force increases the friction force to 183.6 kips (with a $\mu = 0.34$).

3.4.7. Pre-Stress Simulation Results

Figure 33 shows the effects of different pre-stress levels (8.8 kips, 35.2 kips, and 70.4 kips) on the stress range resulting from one lockage cycle. From Figure 33, the retrofit pre-stress level of 8.8 kips does not significantly shift the applied mean stress to have any noticeable impact on the component fatigue life. Higher pre-stress levels at 35.2 kips and 70.4 kips are capable of shifting the mean stress enough to move a portion of the stress range into compression (see Figure 33).

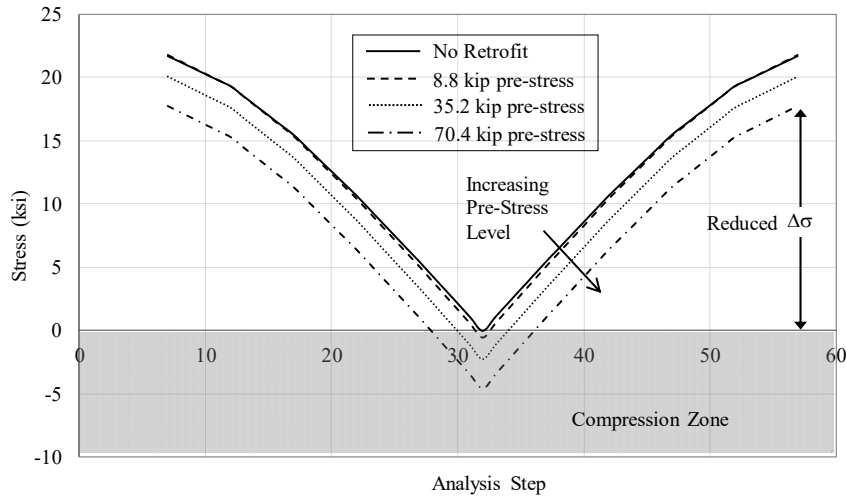


Figure 33. Stress range shift, in Section F13, due to applied CFRP pre-stress (1 lockage cycle)

Both the Goodman constant life diagram and the AASHTO life-cycle fatigue method were implemented using the data from the 3 different pre-stress analyses. The two different methods help determine the effect of the retrofit on the stresses on gate Section F-13. Figure 34 shows a Goodman constant life diagram for Section F-13 with the mean and amplitude stresses of the section with and without the retrofit pre-stress forces. While the pre-stress forces shift the stress state in Section F13 towards the endurance limit, see Figure 34, the applied pre-stress levels are not capable of shifting the component stress states into the infinite life region. Nevertheless, the resulting mean-stress and stress-amplitude shift is capable of extending the fatigue life of the critical gate component.

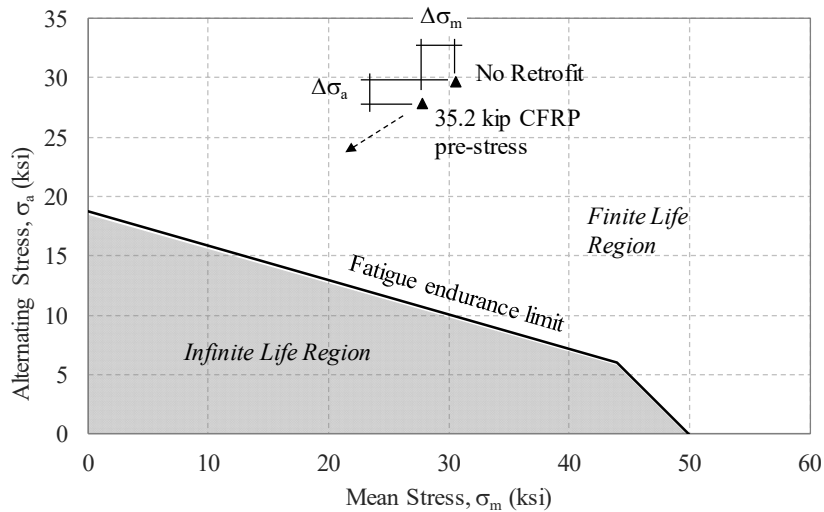


Figure 34. Goodman Life Diagram with stress shift change of Section F13 with the retrofit applying 35.2 kips pre-stress force

Table 4 shows the results of the different pre-stress levels on the resulting fatigue damage in Section F-13. Using the average number of cycles per year for the Greenup Lock and Dam

the cycles can be converted to years of operation. Table 5 shows that the pre-stress force of 35.2 kips extends the life of Section F-13 by 8.6 years (based on an average 3,312.6 annual lockage cycles for the Greenup Lock & Dam Gate 1). Note that with a pre-stress force of 35.2 kips the required friction force considering a bare-steel retrofit on a bare-steel gate component is 51.8 kips, see Appendix E and Equation 11.

Table 4. AASHTO Life-Cycle Fatigue from model data

Pre-Stress Force	Category	Type	# Cycles	$\Delta\sigma$ (ksi)	A (ksi ³)	Δf (ksi)	Nf (cycles)	Total Damage Per Section (SUM (N/Nf))
No Retrofit	E	7.1	1	21.696	1100000000	4.5	107711.1152	9.284E-06
8.8	E	7.1	1	21.800	1100000000	4.5	106169.019	9.419E-06
35.2	E	7.1	1	20.070	1100000000	4.5	136075.3488	7.349E-06
70.4	E	7.1	1	17.762	1100000000	4.5	196297.5537	5.094E-06

Table 5. Stresses from gate model of Greenup Lock & Dam gate 1 (35.2 kip Pre-Stress)

Average Lockages (cycles)	Total Failure Cycles (cycles)	Increase with Retrofit (cycles)	Years to Failure	Increase in life expectancy (yrs.)
3312.6	107711.1	28364.2	32.5	8.6

4. Development of a Fatigue Retrofit Prototype

While the pre-stress required for infinite fatigue life may be impractically large for a retrofit scenario, the analyses indicate that moderate pre-stress levels are capable of significantly extending gate fatigue life (8.6 year extension at 32.5kip pre-stress). In the retrofit development of this study, the pre-stress values considered are chosen to be applied through CFRP plates; however, corrosion precautions must be taken because the CFRP material functions as the cathode in the galvanic reaction with the low-carbon steel anode, promoting steel corrosion. To avoid adverse corrosion effects from the retrofit on the gate component, the CFRP in the retrofit will need to avoid contact with any gate components (forcing an unbonded CFRP retrofit application).

Figure 35 shows the prototype retrofit components, consisting of CFRP clamping plates for loading the CFRP and several friction clamps for transferring the CFRP prestress to the gate section. Also shown in Figure 35 are the retrofit assembly steps. The retrofit prototype constructed in this project is made of A36 steel as a proof of concept; however, in the lock environment, a galvanic protection layer between the steel retrofit and CFRP will be added to prevent galvanic action. Appendix E presents relevant retrofit calculations related to the clamp bolt pretension levels. The CFRP pre-stress is applied by tightening bolts as seen in Figure 36. The retrofit consists of separate parts that fit within the larger friction clamp, seen in Figure 36, to facilitate attachment to the lock gate.

From Figure 36, the bolts bearing on Part (a) of the retrofit apply the pre-stress to the CFRP. The bolts allow Part (b) of Figure 36 to separate from Part (a) creating tension in the CFRP.

The retrofit uses a friction-grip clamping mechanism to keep the CFRP plate from slipping. The grated surfaces increase the coefficient of friction between the metal and CFRP material such that the pre-stress force can be transferred. As the retrofit is clamped the normal forces induced by the bolt pre-tension increases the friction force between the steel retrofit and CFRP

preventing slippage. Figure 37 demonstrates the forces acting within the retrofit to keep the CFRP from slipping.

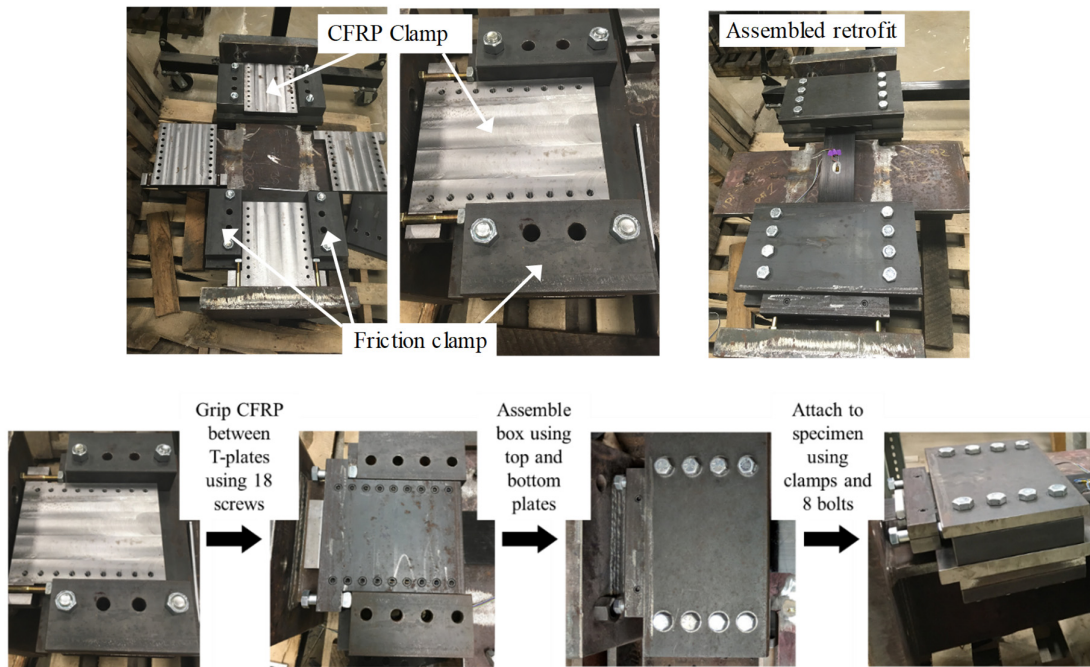


Figure 35. Retrofit components and assembly steps for the CFRP retrofit

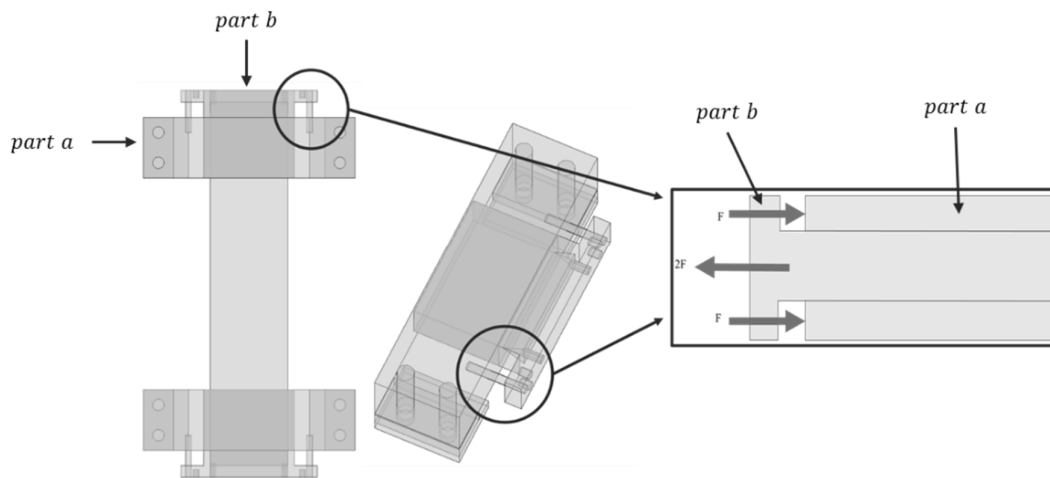


Figure 36. Cross-section of pre-stress bearing mechanism with forces applied by bolts to create the pre-stress

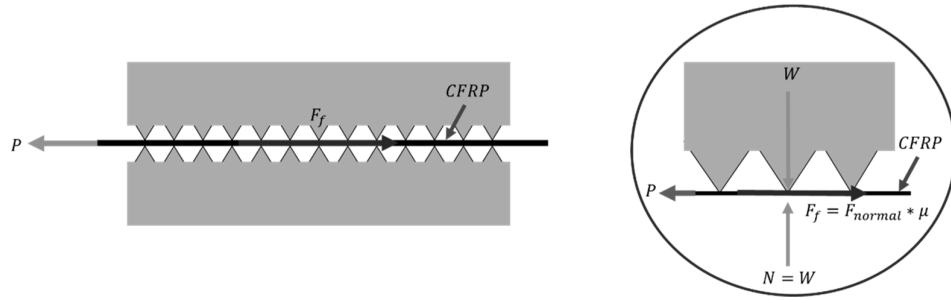


Figure 37. Cross-section view of retrofit friction grip mechanism

4.1. Investigation into Retrofit Bonding Strategies for Achieving Desired Pre-Stress Levels and Preventing Pre-Stress Losses

To transfer the required pre-stress into the gate component, a friction clamping mechanism is designed. The free body diagram shown in Figure 38 is used to assist in the calculation of the friction force required, which is given by Equation 11:

$$F_{friction} = \mu * N \quad \text{Equation 11}$$

where the static coefficient of friction is μ , and N is the normal force. The total required friction force to avoid slippage of the retrofit is one half the required prestress force (see Appendices D and E for additional calculations).

The static coefficient of friction required in Equation 11 is dependent on the interaction between surfaces. Corrosion changes the surface roughness of the steel plate, therefore the static coefficient of friction for an un-corroded and corroded steel plate must be determined, see Figure 39. As shown in Figure 40, an experiment was conducted to determine an estimate for the static coefficient of friction between A36 steel and an uncorroded steel plate and a corroded steel plate. The static coefficient of friction for stainless steel and an uncorroded steel plate was $\mu = 0.297$ and for a corroded steel plate was $\mu = 0.343$, see Appendix A4 for the derivation of static coefficient of friction.

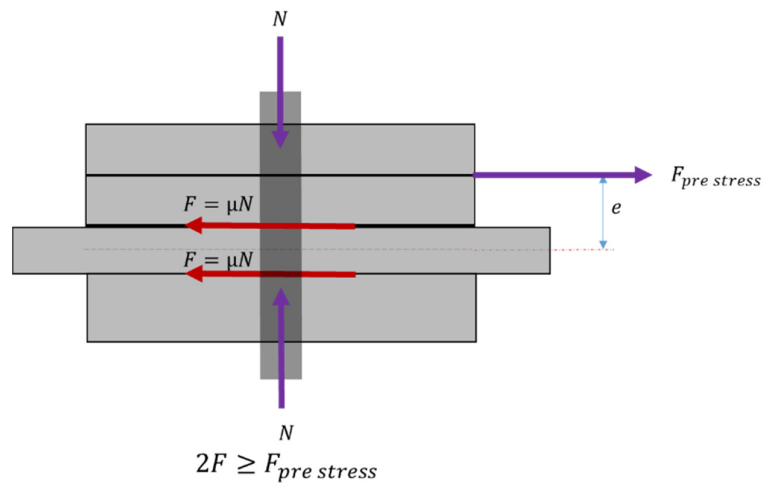


Figure 38. Free body diagram of clamp, retrofit, and section 13 to determine the required friction force from known pre-stress force



Figure 39. Corroded (bottom) and uncorroded (top) steel surfaces

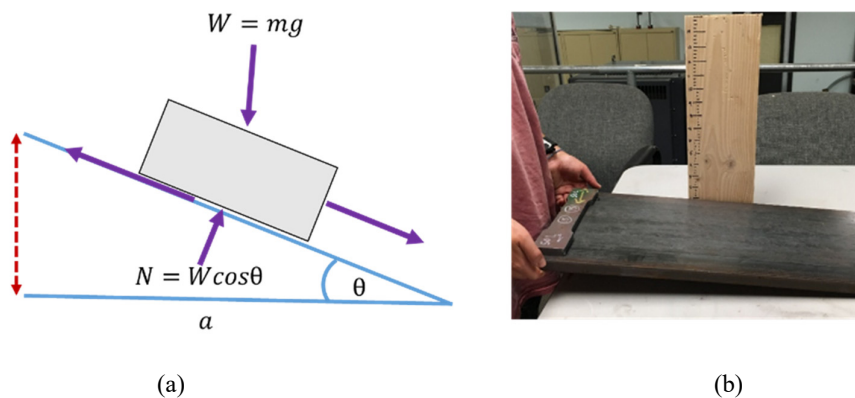


Figure 40. Static coefficient of friction test: a) static coefficient of friction free body diagram; b) test materials

In order for the retrofit to be effective in reducing stresses within the critical gate components, the induced CFRP prestress must be maintained over long durations of time. To investigate the available prestress that can be applied and to understand any prestress losses due to relaxation and creep of the retrofit materials, bonding experiments were conducted for both static slip and longer duration prestress losses. In this study four bonding mechanisms in addition to the bare-steel friction clamps were considered: 1) wedge grips to provide additional clamping of the CFRP, 2) sandpaper to increase the surface roughness and coefficient of friction between the CFRP and steel clamping plates, 3) epoxy adhesion between the steel and CFRP surfaces, and 4) a proprietary Slipnot™ roughened surface created by spraying molten steel on the retrofit clamping surfaces. Figure 41 shows the retrofit clamps with each of the four additional bonding strategies considered.

For each bonding experiment, the CFRP plates and gate component steel surface were instrumented with uni-directional strain gauges for measuring local strains. This allowed prestress levels within the CFRP to be calculated and comparisons between the bonding mechanisms to be made. For each bonding mechanism considered, the initial maximum prestress was obtained by applying increasing prestress levels to the CFRP until the bonding failed (as indicated by a sudden drop in CFRP strain from the gauge readings [see Figure 42]).

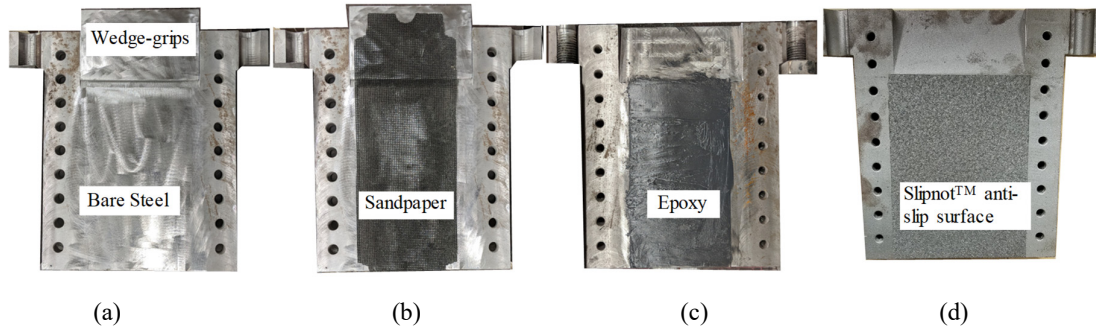


Figure 41. Four bonding mechanisms for clamping the CFRP consisting of: (a) wedge grips, (b) sandpaper, (c) epoxy, and (d) Slipnot™ surface.

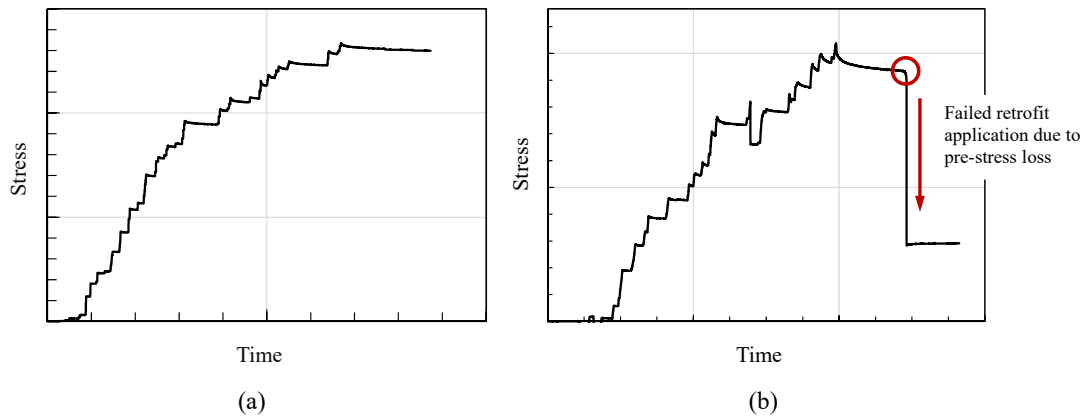


Figure 42. Representation of CFRP stress data showing pre-stress loss due to bond failure.

Table 6 shows the experimental matrix for the bonding experiments, along with the maximum CFRP prestress level achieved. From Table 6, the experiment with only the bare-steel bolted plates achieved 5.03ksi of CFRP prestress prior to initiation of slip between the CFRP and steel surface. By adding the wedge grips, which are designed to clamp the CFRP prior to slip, the maximum prestress achieved at slip was 34.3ksi (nearly seven times that of the bare steel clamps). Additional testing with the clamping wedges and added sandpaper achieved only 15.3ksi of prestress as the flexibility of the sandpaper layer actually reduced the friction between the steel and CFRP. The highest CFRP prestress levels were achieved by using adhesive epoxy to bond the CFRP to the steel clamps. By using an epoxy bond, a CFRP prestress of 52.8ksi was achieved without the CFRP slipping (over ten times that for the bare steel clamped plates). This indicates that the epoxied CFRP bond would likely be able to achieve even higher prestress levels.

Figure 43 shows the prestressing results for the various bonding strategies considered. In Figure 10, it can be seen that the wedge-grip bonding strategy slipped at a CFRP prestress of 34.3ksi while the combined sandpaper and wedge-grip strategy performed worse (only reaching 15.3ksi). From Figure 10, the Slipnot™ and epoxied surfaces performed the best, each being able to achieve more than 50ksi of CFRP prestress. Even though there are similarities in performance between the Slipnot™ and adhesive, a decision was made to proceed with epoxy for the remainder of the structural testing.

Table 6. Test variations to confirm bond mechanism

Bonding Test No.	Plate Clamps	Wedges	Sandpaper	Epoxy	Slipnot™ Surface	Pre-Stress (ksi)
BT-1	X					5.03
BT-2	X	X				34.3
BT-3	X	X	X			15.3
BT-4	X	X		X		52.8
BT-5	X				X	53.8

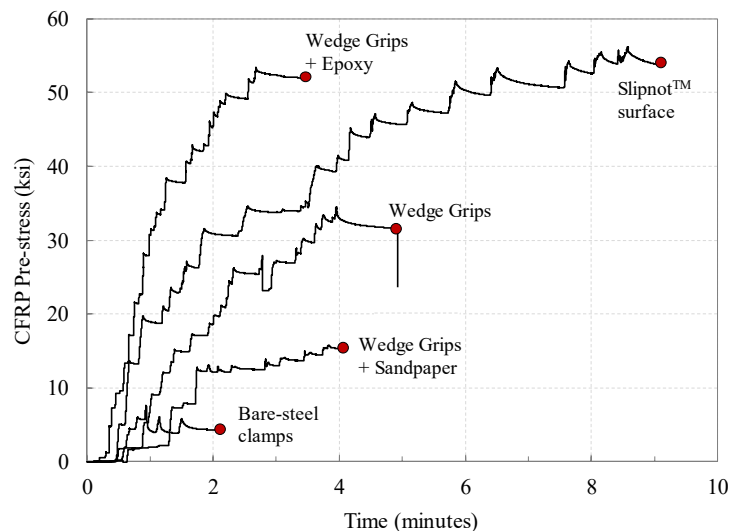


Figure 43. CFRP pre-stress measurements from the different bonding mechanisms considered

While the initial prestress capabilities of the epoxy bonding was chosen based on the initial prestress tests, the long-term effects of prestress loss, specifically creep and relaxation, must be understood to gauge long-term retrofit performance. Long-term tests extended from the static slip tests if there was no failure of the bonding strategy, see Figure 42, which consisted of sandpaper and epoxy. Figure 44 shows the initial prestressing of the epoxied CFRP retrofit, along with the long-term monitoring of prestress losses. From Figure 44, a slight initial prestress loss is observed within the first few minutes. This prestress loss gradually decayed resulting in a total prestress loss of 5.52ksi (approximately 10%) after 14 days. For comparison, prestress losses within the un-epoxied wedge retrofit using sandpaper saw a prestress loss of 1.95ksi (approximately 12%) after 3 days possibly due to the compressibility of the sandpaper.

Because the ambient room temperature can have an effect on prestress measurements, room temperature was recorded during the long-term testing. Figure 45 shows the relationship between CFRP prestress and ambient room temperature during testing of the epoxy-bonded retrofit. In Figure 12, small peaks in CFRP prestress correspond to slight decreases in room temperature.

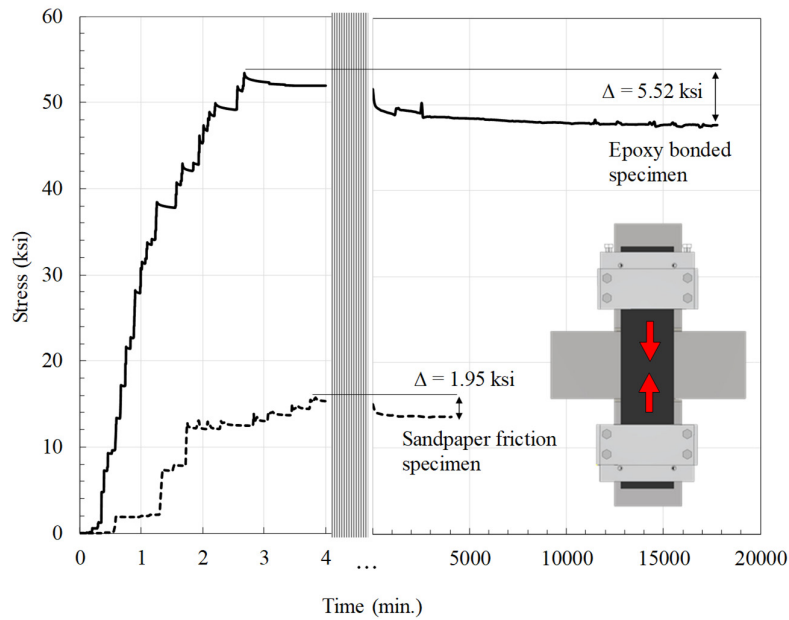


Figure 44. Measured CFRP pre-stress losses due to relaxation and creep.

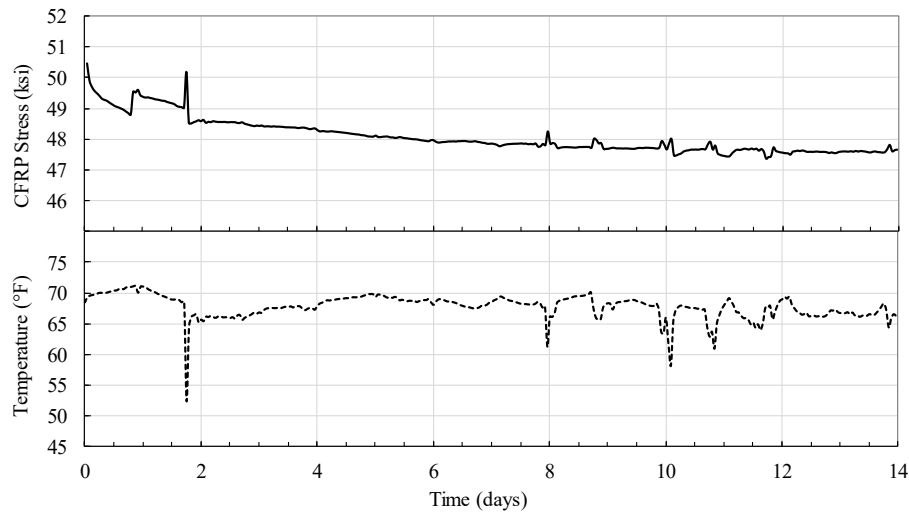


Figure 45. Measured temperature effects on CFRP pre-stress levels.

5. Experimental Investigation into Retrofit Fatigue Mitigation

To verify the effectiveness of the pre-stressing strategy and evaluate the performance of the developed retrofit, seven experimental fatigue tests were conducted. The following sections describe the seven experimental tests, including the test specimen geometry, loading, experimental setup, and instrumentation, followed by a discussion of the testing results.

5.1. Specimen Geometry

Two specimen geometries were considered in the experimental program, one representing a full-scale component geometry and one representing a half-scale component geometry of only the gate faceplate. The full-scale specimen geometry is identical to Section F13 described in Section 3 and is fabricated from design details of the Greenup Lock and Dam provided by the

United States Army Corps of Engineers. Shown in Figure 46(a), the full-scale test specimen is 36 inches by 30 inches by 10-3/4 inches, representing a section of gate near the critical region. Two different weld types join the full-scale test specimen plates. As shown in Figure 46(a), the welds consist of double-sided 3/4in bevel welds and 5/16in. fillet welds. The specimen is designed with two attachment plates connected to each end as seen in Figure 46. These attachment plates are 2in. in thickness to avoid prying effects. Figure 46(b) shows the half-scale specimen dimensions and fabrication details.

All gate specimens tested were notched near the plate intersection welds (see Figure 47) using abrasive cutting discs prior to testing. These notches were added to the specimens to induce local stress concentrations (simulating gate component damage) and to create a worsened fatigue condition.

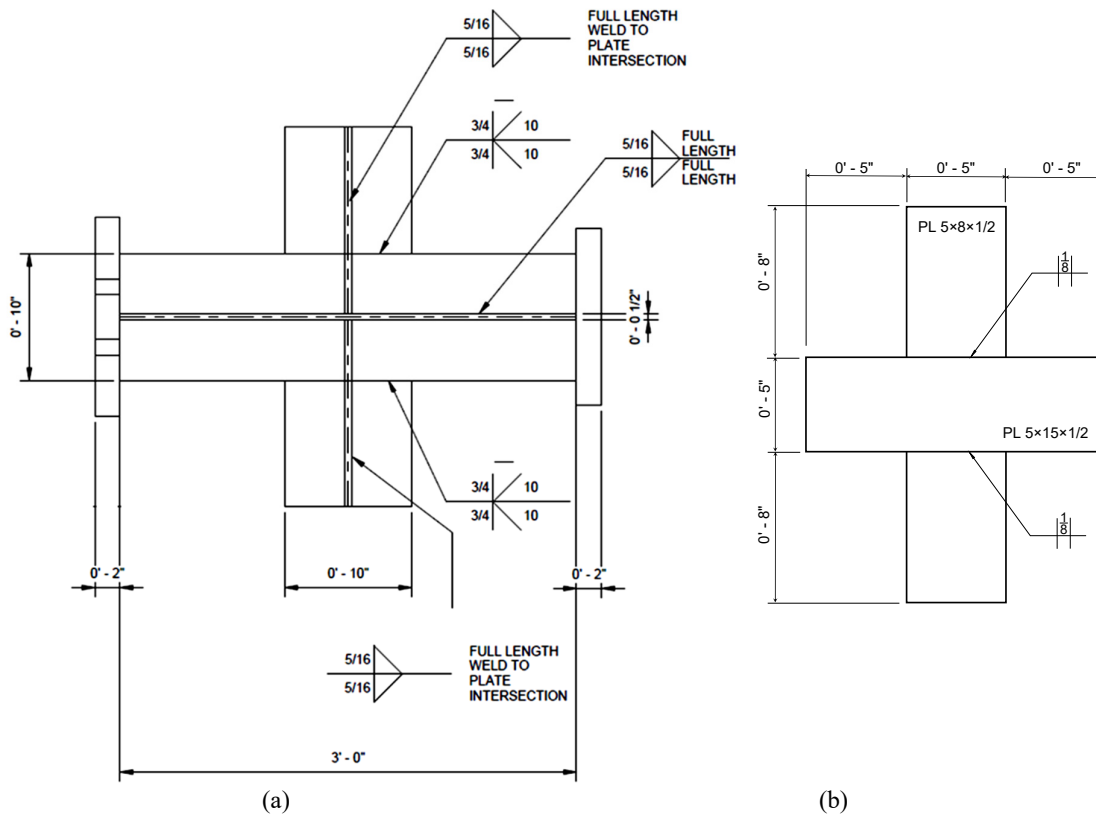


Figure 46. Gate section F13 fabrication details for (a) full-scale specimen and (b) half-scale specimen

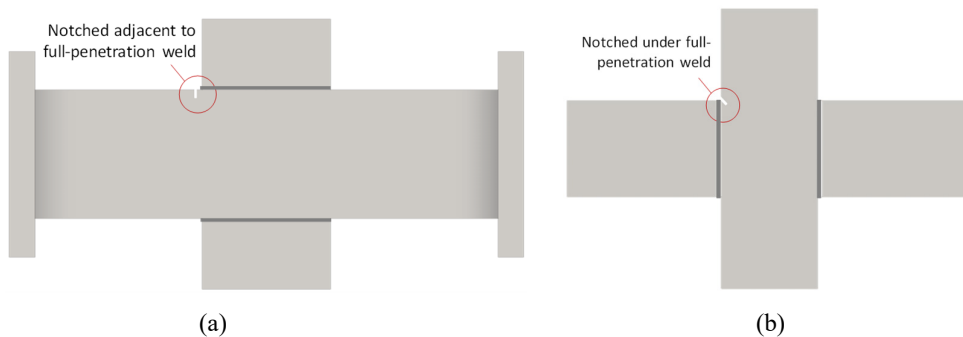


Figure 47. Notch location for (a) full-scale specimen and (b) half-scale specimen.

It is important to note that for the resulting fatigue calculations, this notching reduces the Goodman criteria by dividing the endurance strength, S_e , by a fatigue notch factor, K_f , which is based on the geometry and the elastic stress concentration factor, K_t , of the specimen. The elastic stress concentration factor, K_t , can be calculated from the derived equation shown below [43] which considers the ratio between the depth of the notch, d , and the radius of the notch, r , as shown in Table 7.

$$K_f = 1 + \frac{K_t - 1}{1 + \sqrt{\frac{\rho}{r}}} \rho = \frac{104 \text{MPa}}{S_{ult}}$$

$$K_t = C_1 + C_2 \left(\frac{d}{w}\right) + C_3 \left(\frac{d}{w}\right)^2 + C_4 \left(\frac{d}{w}\right)^3$$

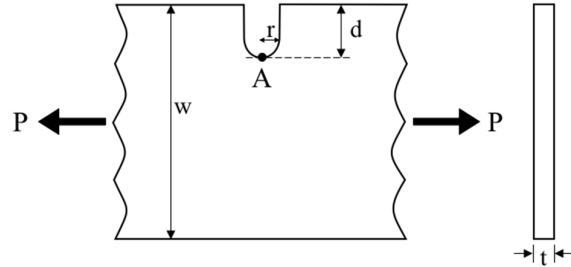


Table 7. Coefficients for stress concentration factor [43]

	$0.5 \leq d/r < 2.0$	$2.0 \leq d/r \leq 20.0$
C1	$0.907 + 2.125\sqrt{d/r} + 0.023 h/r$	$0.953 + 2.136\sqrt{d/r} - 0.005 h/r$
C2	$0.710 - 11.289\sqrt{d/r} + 1.708 h/r$	$-3.255 - 6.281\sqrt{d/r} + 0.068 h/r$
C3	$-0.672 + 18.754\sqrt{d/r} - 4.046 h/r$	$8.203 + 6.893\sqrt{d/r} + 0.064 h/r$
C4	$0.175 - 9.759\sqrt{d/r} + 2.365 h/r$	$-4.851 - 2.793\sqrt{d/r} - 0.128 h/r$

Figure 48 shows how adding notches to the gate specimens reduces the component fatigue endurance limit (see the downward shift of the Goodman line after notching). In Figure 48, it is possible for a notched component to have a finite fatigue life under the same loading conditions that would produce an infinite fatigue life for an un-notched (smooth) component.

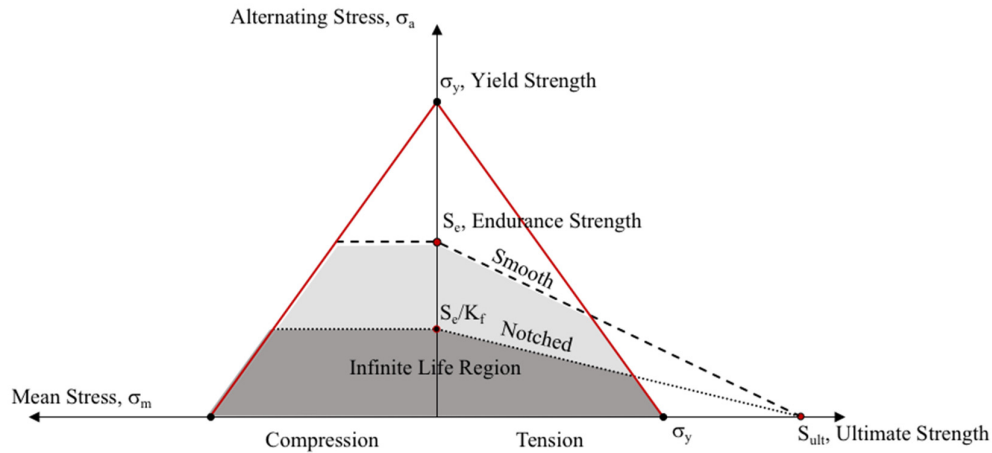


Figure 48. Constant life diagram using the modified Goodman criteria for smooth and notched specimens

5.2. Loading

Constant amplitude unidirectional tensile loading (where the specimen is loaded and unloaded during each cycle) is considered in this study. The loading is intended to simulate similar stress distribution patterns within the gate component during hydrostatic pressure changes

that occur during lock operation. To maintain a constant amplitude nominal stress within the component, all specimens are loaded in force-control. Figure 49 shows the three loading configurations with configuration 1 (C1) representing axial loading of the full-scale gate specimens parallel to the joint welds, configuration 2 (C2) representing bending and shear loading within the full-scale gate specimens, and configuration 3 (C3) representing axial loading of the half-scale specimens perpendicular to the joint weld. It should be noted that during normal gate operation, the gate component feels a combination of bending, shear, and axial load; however, due to limitations with large-scale testing, each of the loading conditions are considered separately.

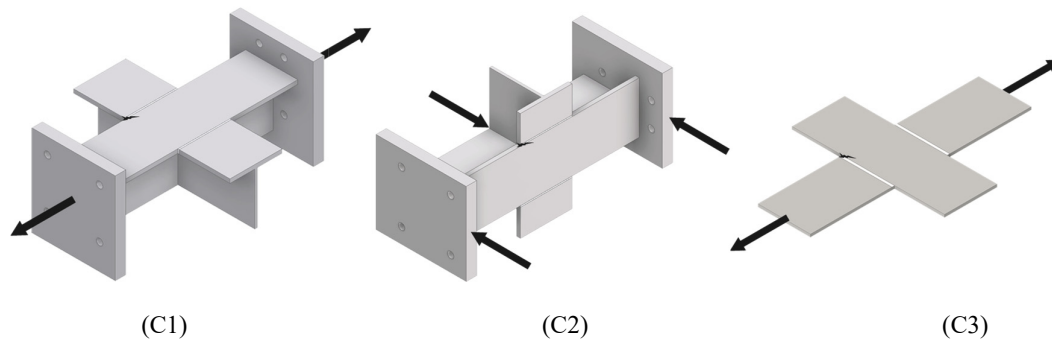


Figure 49. Specimen loading configurations for the full scale component tests (C1 and C2) and the half-scale component tests (C3)

To verify that the loading of the test specimens creates a similar stress state observed during gate operation, a simulation of each test specimen loading was performed. Boundary conditions similar to those imposed by test configurations C1 and C2 are shown in Figure 50, along with a comparison of stress contours between the full gate model and experimental setups. From Figure 50, similar stress concentrations are observed at the test specimen corners while larger stresses are observed near the center of the plate. These larger stresses near the plate center are of less concern from a fatigue standpoint. The stresses near the plate center in the gate model likely differ somewhat from the two test configurations due to the bi-directional bending condition experienced during gate operation. Contours presented in Figure 50 confirm that the two loading configurations impose similar stress conditions near the plate intersection corners.

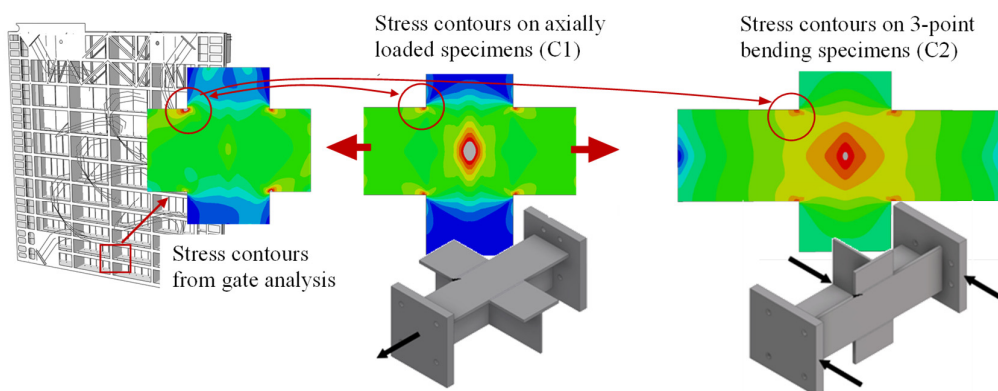


Figure 50. a) Stresses from submodel of Lock Gate; b) Stresses from model of test specimen

5.3. Experimental Setup and Testing Matrix

A total of three full-scale component fatigue tests were conducted on notched gate components to measure the effects of the retrofit strategy near regions of high stress concentration. The full-scale tests consider two loading configurations which induce both axial and flexural stresses in the gate component. Figure 51(a) and Figure 51(b) show the experimental setup for the full-scale testing, consisting of a self-reacting frame, servo-hydraulic actuator, and full-scale gate component specimen. A photograph of the full-scale test setup is also shown in Figure 52(a). The self-reacting frame used to load each gate specimen (shown in Figure 51 and Figure 52) was stiffened for this study to reduce deflections during loading therein allowing higher frequency loadings. The reaction frame consists of two W12×210 beam sections connected to four W12×120 column sections. For axial loading, the specimen is connected to both the actuator and reaction frame (providing an axial load path that must travel through the specimen) with four high-strength 1-1/4" A490 bolts (see Figure 51(a)). For flexural loading, the specimen is subjected to three-point bending subjecting the face of the gate specimen near the critical region to both tension and flexure (see Figure 51(b)).

In addition to the full-scale tests, four half-scale fatigue tests were conducted to investigate alternative specimen orientations and the effectiveness of the prestressed retrofit on fatigue crack mitigation. Unlike the full-scale specimens, all half-scale specimens are tested in a Walter+Bai servo-hydraulic bi-axial fatigue testing machine capable of providing rapid fatigue cycles. Figure 51(c) shows the half-scale testing configuration and Figure 52(b) shows a photograph of the half-scale specimen during testing. Table 8 presents the experimental testing matrix, outlining the specimen names, retrofit condition, loading type, applied force range, and retrofit prestress level (if applicable).

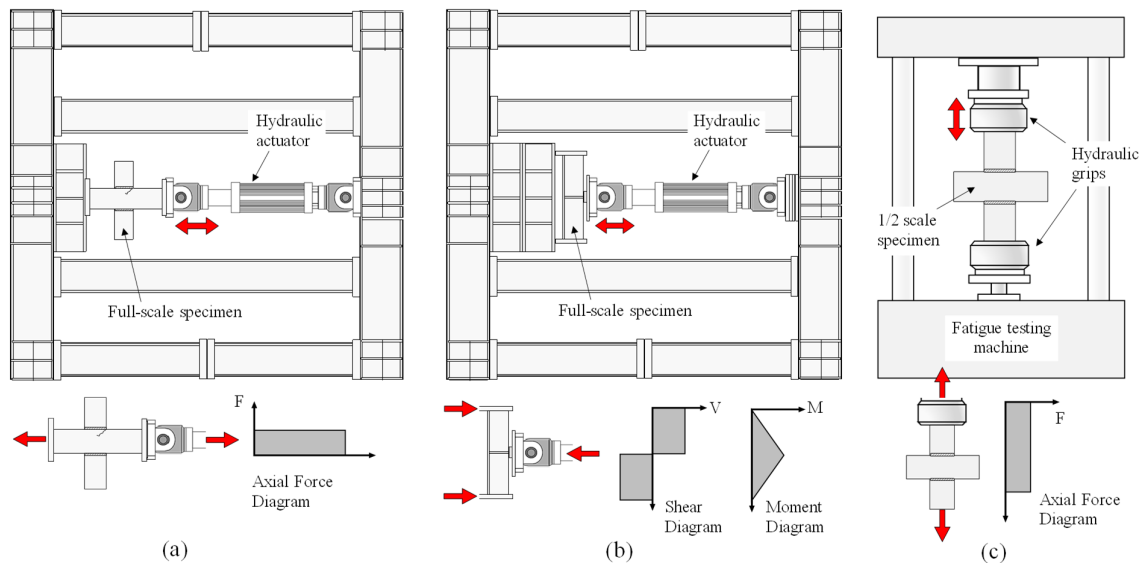


Figure 51. Experimental test setup and specimen force diagrams for (a) full-scale axially loaded specimen, (b) full-scale specimen in three-point bending, and (c) half-scale axially loaded specimen.

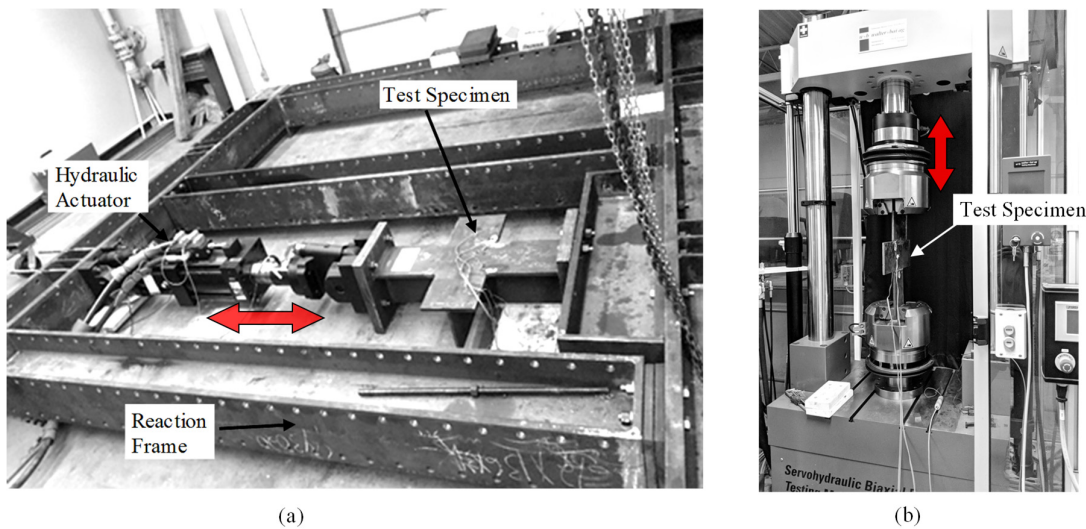


Figure 52. Photograph of experimental setup for (a) full-scale testing in the large reaction frame and (b) half-scale testing in the Walter+Bai servo-hydraulic bi-axial fatigue testing machine

Table 8. Experimental test matrix

Experimental test No.	Retrofit (Y/N)	Loading type	Loading frequency (Hz)	Applied force range (kips)	Applied retrofit pre-stress level (ksi)
C1-1	N	Axial	2 – 6	50 – 80	--
C2-1	N	3-point	2 – 6	80	--
C2-2	Y	3-point	2 – 6	80	7.3 – 17.3
C3-1	N	Axial	2	19.6	--
C3-2	Y	Axial	2	19.6	7.2 – 18.0
C3-3	N	Axial	2 – 8	19.6	--
C3-4	Y	Axial	2 – 8	19.6	13.65

5.4. Instrumentation and Monitoring

Each experimental specimen was instrumented with multiple strain gauges to monitor local component stresses during loading. These gauges were located near the notched regions to measure local stress concentrations resulting from the geometry discontinuities, as well as regions away from any local influences to measure nominal specimen stresses. Figure 53 shows the orientation and location of instrumentation for the C1, C2, and C3 specimen configurations. Note that gauges are provided on both sides of the steel plate to allow for separation of measured bending and axial stresses.

In addition to the instrumentation, non-destructive monitoring techniques were used to identify and track the presence of fatigue cracking. The crack detection method used in this study involves visual inspection aided by dye penetrant. It should be noted that while the dye penetrant was the primary means for identifying crack initiation, post-test analysis of the strain gage data also helped in identifying the presence of cracking through measurement of local force changes.

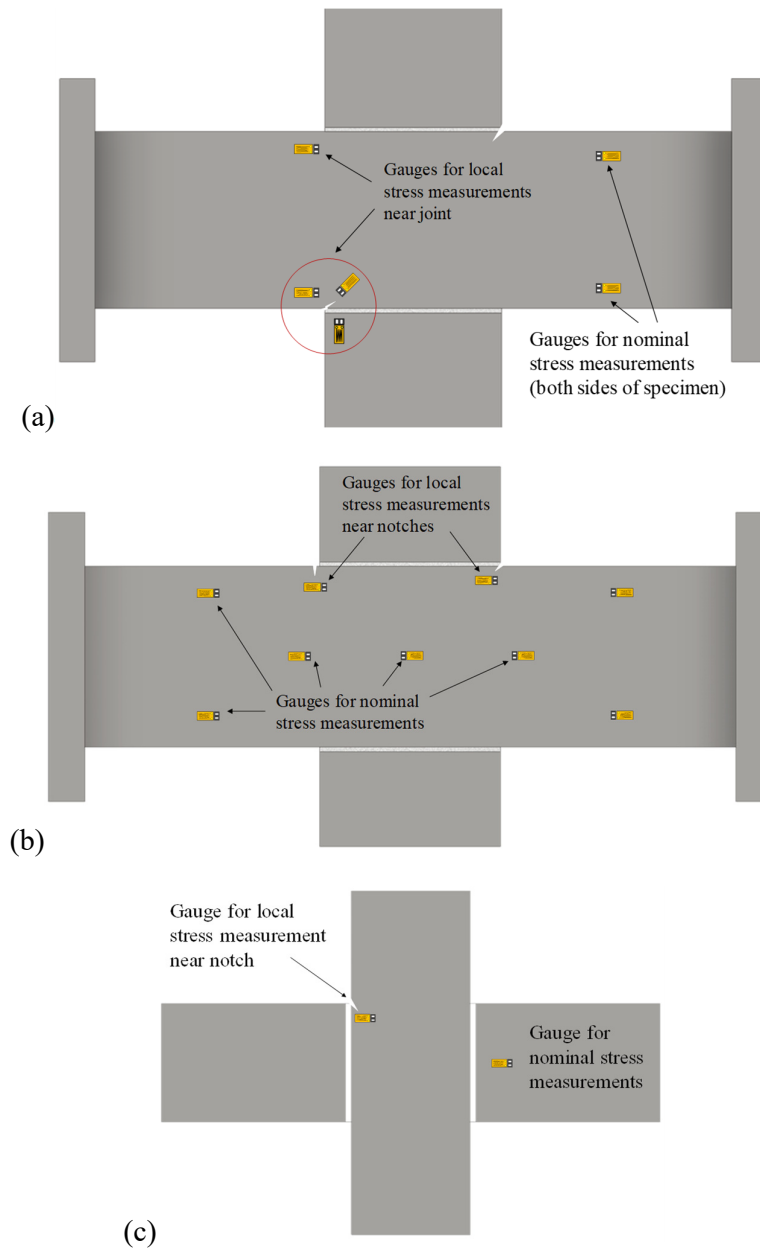


Figure 53. Strain gage locations for the various specimen configurations: (a) full-scale axial, (b) full-scale 3-point, and (c) half-scale axial.

5.5. Experimental Fatigue Test Results

5.5.1. Testing Observations from Full-Scale and Half-Scale Specimens

As mentioned in the description of specimen geometry, all specimens were notched near a weld corner to aid in crack initiation and simulate poor detailing (common in many existing gate components). Preliminary testing was conducted on specimen C1-1 to measure the effect of this notching on the local stress-state near the connection weld region. Figure 54 compares the pre- and post-notch stresses within the connection region of specimen C1-1 which indicates that the notching increases the local stress state by more than 4.5 times. Note that the gauge results presented in Figure 54 are averages between gauges on the top and bottom

plate sides (to isolate axial strains). By comparing the top and bottom longitudinal gauges in Figure 54(a), It can be observed that the experimental loading induced slight lateral bending in the specimen (note that the solid line from the top gauge is larger than the dashed line from bottom gauge).

Following notching of specimen C1-1, a total of 13,730,163 fatigue cycles were applied at a force range of 50kips with no observable fatigue cracking near the notch. Strain measurements near the notch remained stable throughout the test and resembled those shown in Figure 21(b) indicating no fatigue cracking. Additional dye-penetrant testing near the notch helped confirm no fatigue cracking by visual inspection. Due to the significant time required to generate a fatigue crack, it was decided to conclude the axial loading fatigue test and focus on the three-point bending specimen configuration capable of producing higher stresses within the gate specimens.

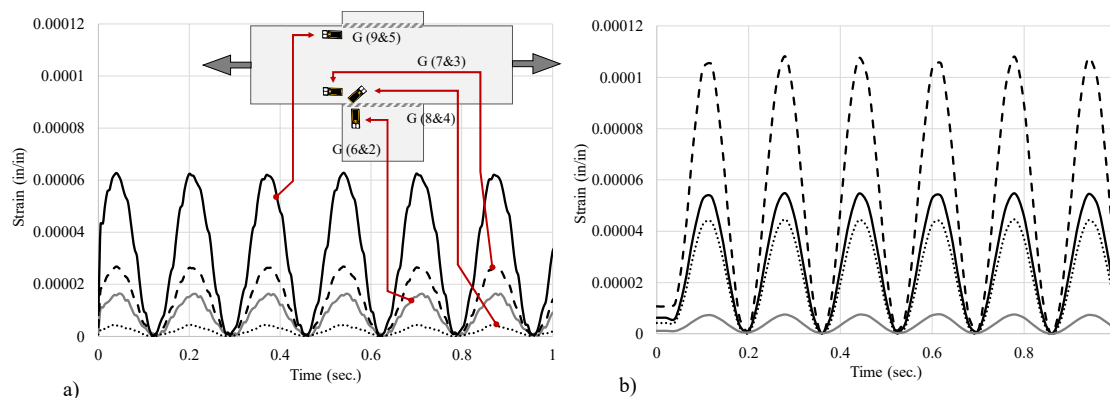


Figure 54. Recorded strains, a) pre-notch; b) post-notch

The goal of the initial fatigue testing with specimens C1-1 and C2-1 was to induce a sharp fatigue pre-crack to investigate retrofit effectiveness; however, similar to specimen C1-1, specimen C2-1 (loaded in three-point bending at a force range of 80kips) was subjected to 4,598,234 fatigue cycles with no observable fatigue crack forming at the notch. Rather than continue with the fatigue crack initiation experiments, it was decided to use the local stress concentration from the induced notch to investigate the local stress effects of the prestressed retrofit. Table 9 shows the additional cyclic tests conducted (C2-2, C3-1, and C3-2) to provide comparison between local notch stress states without and with various levels of CFRP prestress. Tests C3-3 and C3-4 were added half-scale fatigue tests to measure resulting fatigue-life improvements and will be discussed in a later section.

Table 9. Experimental test matrix and resulting fatigue cycles applied

Experimental test No.	Retrofit (Y/N)	Loading type	Retrofit pre-stress level (ksi)	Number of applied fatigue cycles
C1-1	N	Axial	--	13,730,163
C2-1	N	3-point	--	4,598,234
C2-2	Y	3-point	7.3-17.3	N/A
C3-1	N	Axial	--	N/A
C3-2	Y	Axial	7.2-18.0	N/A
C3-3	N	Axial	--	989,235
C3-4	Y	Axial	13.65	2,911,198

5.5.2. Effect of Retrofit Pre-Stress Levels on Specimen Local Stresses

The applied CFRP prestress is capable of reducing the local stress felt at the notch of both the full-scale and half-scale specimens. Table 10 presents the three full-scale and four half-scale experiments having varied levels of CFRP prestress. In Table 10, prestress levels ranging between 7.3 and 17.3ksi were able to reduce the full-scale component mean stress by between 4 and 8.3ksi. Additionally, the prestress was able to reduce the stress-amplitude of the full-scale notch stress by between 1.6 and 2.3ksi. Similar results were observed for the half-scale experiments, with prestress levels between 7.2 and 18ksi reducing the component mean stress by between 2.5 and 5.4ksi respectively. The reduction in mean stress and stress-amplitude at the notch directly translates to increased fatigue life. Figure 55 shows the effect of prestress level on stress-range and mean stress for the full-scale experiments. In Figure 55, a noticeable downward shift can be seen as the prestress level in the CFRP is increased.

Table 10. Mean and amplitude stress shift due to CFRP pre-stress level

Specimen Type	Applied force range (kips)	Retrofit pre-stress level (ksi)	Reduction in component mean stress (ksi)	Reduction in component stress amplitude (ksi)
Full-Scale	50-80	7.30	4.0	1.6
Full-Scale	80	14.8	7.7	2.2
Full-Scale	80	17.3	8.3	2.3
Half-Scale	19.6	7.20	2.5	0.7
Half-Scale	19.6	10.6	3.4	1.2
Half-Scale	19.6	12.5	4.0	1.5
Half-Scale	19.6	18.0	5.4	2.3

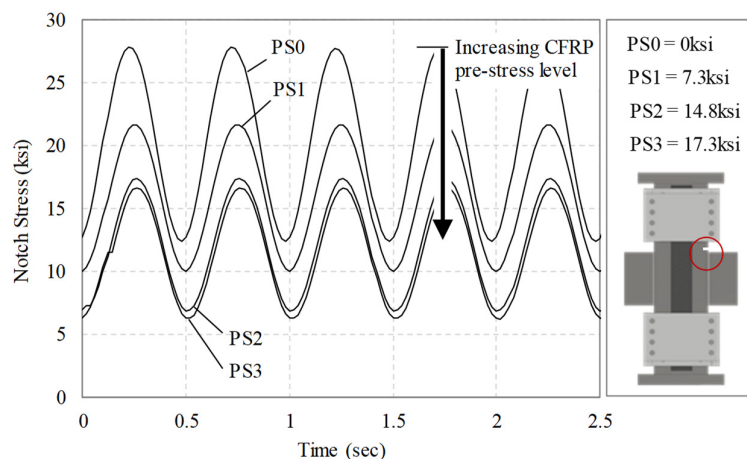


Figure 55. Effect of CFRP pre-stressing on notch local stress history

As the specimen notch stress is reduced, the stress-state moves closer to the infinite life region. For the full-scale and half-scale experiment, the resulting shift in notch stress state relative to the notched Goodman criterion is shown in Figure 56 and Figure 57 respectively. As shown in Figure 56, the 8.3ksi reduction in mean stress at a prestress of 17.3ksi shifts the notch stress-state near the border of the fatigue threshold line, but remains within the finite life region. This indicates that a fatigue life improvement is likely made; however, the

component will eventually be subject to fatigue cracking. Similar results were noticed for the half-scale specimens which remained within the finite life region after achieving a mean-stress shift of 5.4ksi at 18ksi prestress. The following section quantifies the effect of this mean stress shift on the resulting half-scale component fatigue life.

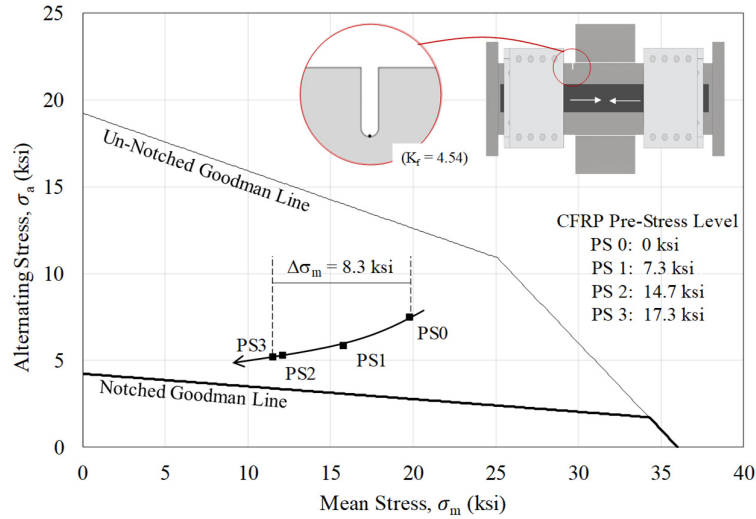


Figure 56. Effect of CFRP pre-stress level on full-scale component stress state

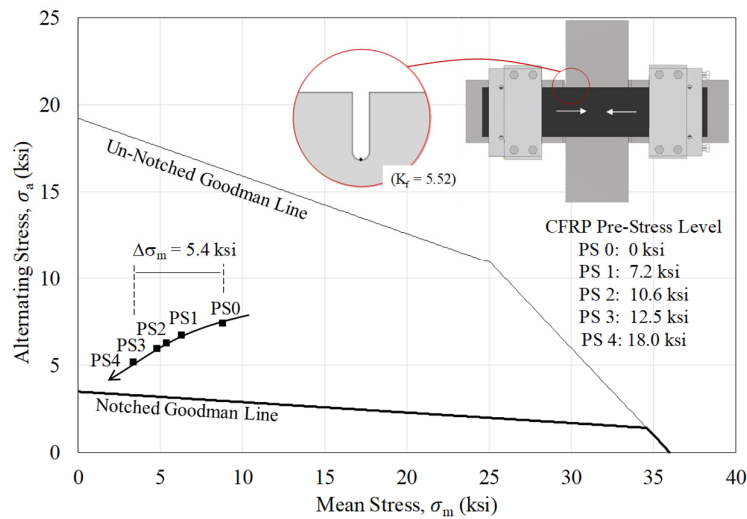


Figure 57. Effect of CFRP pre-stress level on small-scale component stress state

5.5.3. Effect of Pre-Stressed Retrofit on Specimen Fatigue Life

The effect of the developed retrofit on resulting fatigue life is determined by comparing the fatigue performance of specimen C3-3 (having no retrofit) and C3-4 (having a retrofit and 13.65ksi prestress). Specimen C3-3 with no retrofit experienced fatigue cracking at the notch which resulted in complete cross-section fracture after 989,235 cycles. Considering a fatigue category E' detail, a notched weld, specimen C3-3 would be calculated to fail after 969,165

cycles which is fairly close to the experimental observation. Figure 58 shows the resulting fatigue fracture emanating from the induced notch. Application of the retrofit in specimen C3-4 increased the number of cycles to failure for the half-scale gate specimen to 2,911,198 cycles (a fatigue life increase of nearly 3 times over the un-retrofitted specimen). Figure 59 shows a comparison of the stress within the notch for the specimens C3-3 (un-retrofitted) and C3-4 (retrofitted), with the reduced notch stress resulting in increased fatigue life. In Figure 59, application of the retrofit initially decreased the notch stress by 20.5ksi as compared to the unretrofitted specimen C3-3. Note however that the retrofit did not perform as well as intended, due to a prestress loss that was observed at 50,000 cycles which resulted in an increase in notch stress (see Figure 59). This prestress loss was due to a debonding failure between the friction clamps and half-scale specimen and was corrected at 1,000,000 cycles during testing but eventually was lost again at 1,690,000 cycles. This prestress loss will be discussed further in the following section; however, it should be noted that even with prestress losses, the CFRP continued to take load resulting in a reduced notch stress of nearly 4.8 ksi (see Figure 59).

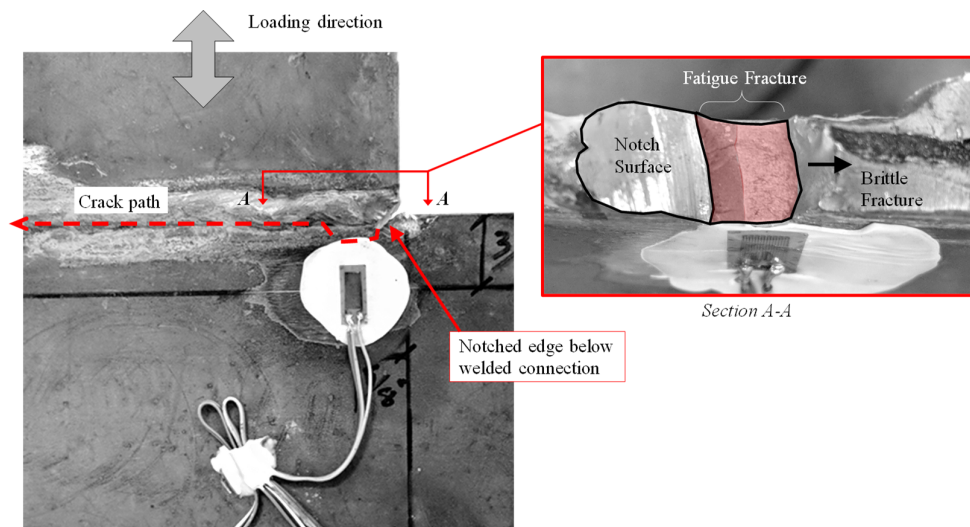


Figure 58. Fatigue crack growth and eventual brittle fracture of specimen C3-3 following 989,235 cycles.

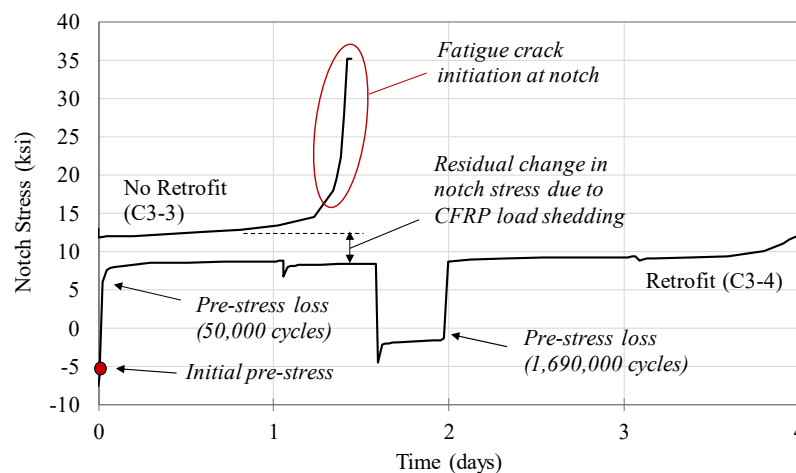


Figure 59. Measured stress at the notch of specimen C3-3 (no retrofit) and specimen C3-4 (retrofit)

5.5.4. Performance of Half-Scale Retrofit Clamping Mechanisms during Cyclic Loading

While the static retrofit bonding experiments were promising for inducing CFRP prestress levels up to 50ksi, vibrations during rapid cyclic loading ultimately affected the retrofit bond and resulting CFRP prestress within the retrofit system. Epoxy debonding between the retrofit and gate specimen was observed in each high-cycle fatigue test. As an example, Figure 60 shows the CFRP prestress levels during the half-scale test C3-4 (discussed previously), where the initial prestress of 13.7ksi was reduced by 11.8ksi following approximately 50,000 cycles at 20Hz (41 minutes of loading) due to debonding of the retrofit clamps from the specimen surface. Following 1,000,000 cycles, an additional prestress was performed to 10.15ksi by allowing the debonded retrofit clamp to bear on the specimen weld profile, which resulted in the other retrofit clamp to debond after an additional 690,000 cycles (9 hours and 35 minutes of testing in Figure 60). Note that even though the retrofit clamps debonded, the CFRP material continued to take some of the applied axial load (equal to the applied clamping friction force). Given the results of the epoxy performance during fatigue loading, future retrofit performance may be improved by using the Slipnot™ surface which had similar static prestress results but relies on friction over adhesion to maintain CFRP prestress levels.

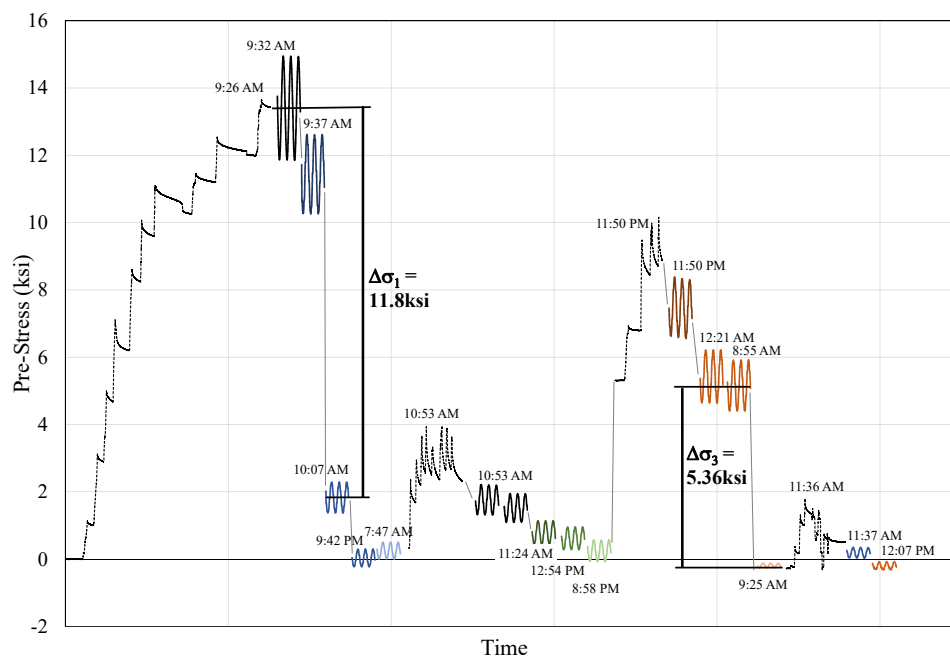


Figure 60. Measured CFRP pre-stress during rapid cyclic loading.

Implementation plans for the developed retrofit strategy on an existing lock gate was postponed by the USACE during the 2018 project year. Efforts are currently underway and coordination meetings have already been held to implement the pre-stressed CFRP retrofit in a bonded configuration with the CFRP glued directly to the gate steel surface, to overcome the eventual pre-stress losses due to CFRP slip during cyclic loading. Implementation and monitoring of the developed fatigue retrofit will likely take place during the 2019 calendar year.

6. Summary and Conclusions

This study analytically and experimentally investigated fatigue damage within common lock gate geometries, and developed fatigue mitigation strategies using tuned pre-stress levels to extend gate service-life. In this study, detailed finite element analyses were used to identify critical lock gate fatigue regions and evaluate pre-stress effects on locally extending component fatigue life. Fatigue and fracture mechanics theories related to constant life diagrams were used to develop retrofit strategies for preventing fatigue cracking and full-scale experimental fatigue testing of a critical lock gate component was conducted to provide a baseline for evaluation of retrofit strategies. Retrofit strategies using carbon fiber reinforced polymer (CFRP) plates having optimized pre-stress levels were created and fatigue tested in laboratory conditions. The following conclusions result from the analytical and experimental study:

- Fatigue analyses determined gate Section F13 of the Greenup Lock and Dam (see again Figure 22), as the critical fatigue region. This gate detail geometry is common in much of the US inland waterway lock gate infrastructure.
- Considering only the outer flange when determining the required pre-stress level for infinite fatigue using the Goodman Constant Life Diagram results in an inaccurately low estimation of required retrofit pre-stress (the required prestress force of 8.8 kips was determined as too low from finite element and fatigue evaluations). The likely cause is prestress force lag into adjacent component stiffeners.
- Considering the stiffened component geometry results in a more accurate estimate of required prestress; however, the required value for the Greenup Lock and Dam is impractically large to apply in a retrofit situation (for infinite life a prestress force of 366.6 kips was required).
- Pre-stress levels lower than those required for infinite life are still capable of extending gate life by several years. Analytical gate simulations indicate that a pre-stress force of 35.2 kips extends the fatigue life of Section F13 in the Greenup Lock & Dam Gate by 8.6 years.
- Application of the pre-stressed retrofit on the notched half-scale specimen increased the fatigue life by more than 1.9 million cycles (a fatigue life increase of nearly 3 times over the un-retrofitted specimen).
- Pre-stressing strategies considering friction alone can achieve CFRP pre-stress levels similar to those with epoxy adhesives. The Slipnot™ high friction coating and epoxy bonded CFRP both achieved similar pre-stress levels prior to slip at slightly more than 50 ksi of CFRP pre-stress.
- Creep and relaxation within the pre-stressing system contributed to minor pre-stress losses. The full-scale epoxy-bonded CFRP specimen converged to approximately 10% pre-stress loss after 14 days.
- The applied CFRP pre-stress is capable of reducing the local stress felt at the notch of both the full-scale and half-scale specimens; however, pre-stress loss did occur due to epoxy adhesive debonding during rapid cyclic loading.

- Load shedding into the CFRP, even without significant pre-stress applied, contributed to reductions in component notch stresses. Even after debonding, the applied CFRP clamping force was able to provide enough force transfer to the CFRP to reduce the notch local stresses (see again Figure 59).

REFERENCES

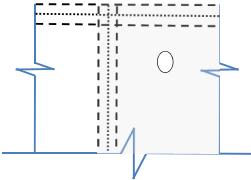
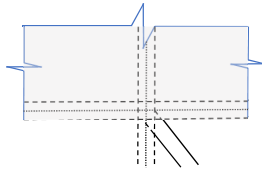
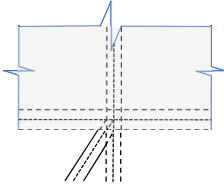
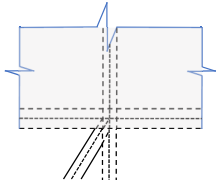
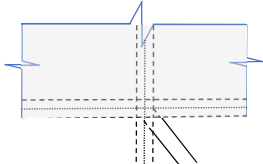
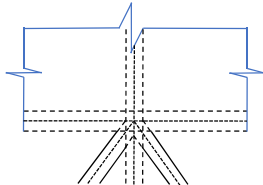
- [1] USACE (1999). "Inland Waterway Navigation: Value to the Nation," *US Army Corps of Engineers*, Institute for Water Resources.
- [2] PPC (2017). "The port district and the inland waterway system," *The Port of Pittsburgh Commission*, Retrieved December 2017 from: <http://www.port.pittsburgh.pa.us/index.aspx?page=127>.
- [3] USACE (2016). "Illinois Waterway Locks and Dams: Rock Island District," *US Army Corps of Engineers*, Mississippi Valley Division.
- [4] USDOT (2011). "America's Marine Highway Report to Congress," *US Dept. of Transportation Maritime Administration*, April, 2011.
- [5] ASCE (2017). "Infrastructure Report Card: Inland Waterways," *American Society of Civil Engineers (ASCE)*.
- [6] D. V. Grier (2017). "The Declining Reliability of the U.S. Inland Waterway System," *Homeland Security Digital Library*, US Army Corps of Engineers, Institute for Water Resources.
- [7] P. Glass (2012). "Head Lock," *Work Boat*, accessed July 2, 2018 from <https://www.workboat.com/archive/head-lock/>.
- [8] USACE (2005). "McAlpine Lock Closure in August 2004," *The Navigation Economic Technologies Program*, IWR Report 05-NETS-R-08.
- [9] J. Brinckman (2009). "Dam's lock closure hurts Northwest shippers but could have been far worse," *The Oregonian*, Accessed July 2, 2018 from: https://www.oregonlive.com/business/index.ssf/2009/10/post_1.html.
- [10] B. Chapman (2010). "LRD's lock gate replacement program," *Presentation slides to the Inland Waterways User Board*, Oct 20, 2010.
- [11] D. A. Jones (1992). "Principles and Prevention of Corrosion," *Macmillan Publishing Co.*, New York, New York.
- [12] R. S. Prem Pal Bansal, Ankur Mehta (2016). "Retrofitting of RC girders using pre-stressed CFRP sheets," *Steel and Composite Structures*, 20(4). 833-849.
- [13] R. A.-M. Alaa AL-Mosawe, Xiao-Ling Zhao (2015). "Effect of CFRP properties on the bond characteristics between steel and CFRP laminate under quasi-static loading," *Construction and Building Materials*, 98(489-501).
- [14] P. B. Prem, Sharma, R., and Mehta, A. (2016). "Retrofitting of RC girders using pre-stressed CFRP sheets," *Steel and Composite Structures*, 20(4).

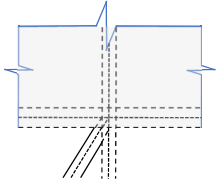
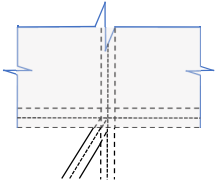
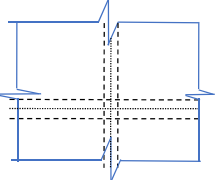
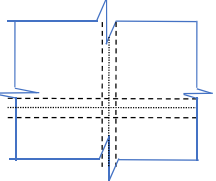
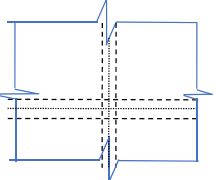
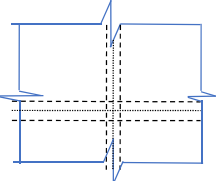
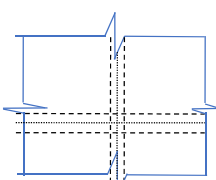
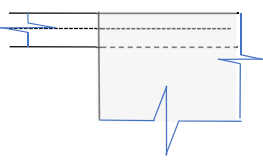
- [15] A. Al-Mosawe, Al-Mahaidi, R., and Zhao, X.L. (2015). "Effect of CFRP properties, on the bond characteristics between steel and CFRP laminate under quasi-static loading," *Construction and Building Materials*, 98(2015). pp. 489-501.
- [16] H. Mahmoud, Riveros, G., Memari, M., Valsangkar, A., and Ahmadi, B. (2018). "Underwater Large-Scale Experimental Fatigue Assessment of CFRP-Retrofitted Steel Panels," *J. Struct. Eng.*, 144(10).
- [17] F. Matta, Aquino, C., Nanni, A., Giancaspro, J. (2007). "Unbonded CFRP bar system for external post-tensioning," *Proc. Composites and Polycon 2007*, October 17-19, Tampa, FL.
- [18] E. Ghafoori, Prinz, G.S., Nussbaumer, A., Motavali, M., Herwig, A., and Fontana, M. (2014). "Finite element analysis for fatigue damage reduction in metallic riveted bridges using pre-stressed CFRP plates," *Polymers*, 6(4). pp.1096-1118.
- [19] S. Hong, and Park, S.-K. (2015). "Concrete beams strengthened with prestressed unbonded carbon-fiber-reinforced polymer plates: An experimental study," *Polymer Composites*, 38(11).
- [20] T. L. Anderson (2004). "Fracture Mechanics: Fundamentals and Applications, 3rd Edition," *CRC Press LLC*, ISBN: 978-0-84-931656-2.
- [21] D. Mertz (2012). "Steel Bridge Design Handbook: Design for Fatigue," *US DOT FHWA*, Publication No. FHWA-IF-12-052-Vol. 12.
- [22] AASHTO (2012). "AASHTO LRFD bridge design specifications (6th edition)," *American Association of State Highway and Transportation Officials*, Washington, DC.
- [23] R. J. Dexter, and Ocel, J.M. (2013). "Manual for repair and retrofit of fatigue cracks in steel bridges," *Report No. FHWA-IF-13-020*.
- [24] S. Caramelli, Croce, P., and Froli, M. (1997). "Repair techniques for the rehabilitation of fatigue cracked orthotropic steel bridges," *International Association for Bridge and Structural Engineering (IABSE) reports*, 76(1997). pp. 161-169.
- [25] K. Yamada, Sakai, Y., Kondo, A., and Kikuchi, Y. (1986). "Weld repair of cracked beams and residual fatigue life," *Structural Eng. / Earthquake Eng. (JSCE)*, 3(2). pp. 373s-382s.
- [26] J. M. O. Robert J. Dexter "Manual for Repair and Retrofit of Fatigue Cracks in Steel Bridges," U.S. Department of Transportation Federal Highway Administration.
- [27] E. Ghafoori, Motavalli, M., Nussbaumer, A., Herwig, A., Prinz, G.S., and Fontana, M. (2015). "Design criterion for fatigue strengthening of riveted beams in a 120-year-old railway metallic bridge using pre-stressed CFRP plates," *Composites: Part B*, 68(2015). pp. 1-13.
- [28] E. Ghafoori, Motavalli, M., Herwig, A., Nussbaumer, A., Prinz, G.S., and Fontana, M. (2016). "Fatigue strengthening of riveted girders in a historic railway metallic bridge in Switzerland using pre-stressed un-bonded CFRP laminates," *Proc. 8th International*

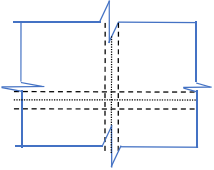
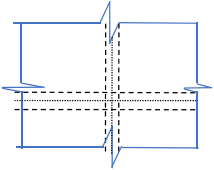
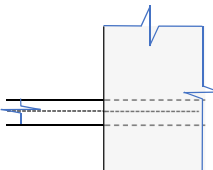
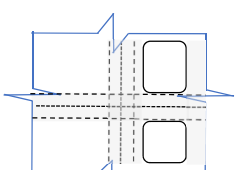
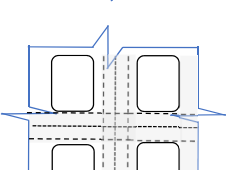
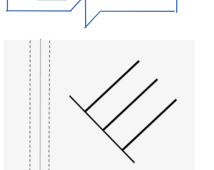

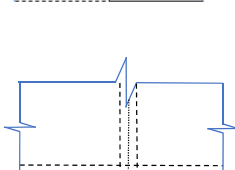
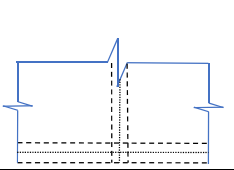
- Conference on Bridge Maintenance, Safety and Management (IABMAS)*, Foz do Iguaco, Brazil.
- [29] M. Tavakkolizadeh, and Saadatmanesh, H. (2003). "Fatigue Strength of Steel Girders Strengthened with Carbon Fiber Reinforced Polymer Patch," *J. Struct. Eng.*, 129(2).
- [30] T. Alkhrdaji (2015). "Strengthening of Concrete Structures Using FRP Composites," *Structure Magazine*, June(2015). pp. 18-20.
- [31] A. Peiris, and Harik, I. (2015). "Steel Bridge Girder Strengthening Using Postinstalled Shear Connectors and UHM CFRP Laminates," *J. Performance of Constructed Facilities*, 29(5).
- [32] D. Schnerch, and Rizkalla, S. (2008). "Flexural Strengthening of Steel Bridges with High Modulus CFRP Strips," *J. Bridge Eng.*, 13(2).
- [33] T. C. Miller, Chajes, M.J., Mertz, D., and Hastings, J.N. (2001). "Strengthening of a Steel Bridge Girder Using CFRP Plates," *J. Bridge Eng.*, 6(6).
- [34] B. Kaan, Alemdar, F., Bennett, C., Matamoros, A., Barrett-Gonzalez, R., and Rolfe, S. (2012). "Fatigue Enhancement of Welded Details in Steel Bridges Using CFRP Overlay Elements," *J. Composites for Construction*, 16(2).
- [35] Y. Huawen, Konig, C., Ummenhofer, T., Shizhong, Q., and Plum, R. (2010). "Fatigue Performance of Tension Steel Plates Strengthened with Prestressed CFRP Laminates," *J. Composites for Construction*, 14(5).
- [36] H. Mahmoud, Chulahwat, A., and Riveros, G. (2018). "Fatigue and fracture life-cycle cost assessment of a Miter gate with multiple cracks," *Engineering Failure Analysis*, 83(2018). pp. 57-74.
- [37] E. Ghafoori, and Motavalli, M. (2011). "Analytical calculation of stress intensity factor of cracked steel I-beams with experimental analysis and 3D digital image correlation measurements," *Eng. Fracture Mech.*, 78(18). pp. 3226-42.
- [38] HKS (2006). "ABAQUS Standard Users manual, Version 6.4," Hibbitt, Karlsson, and Sorensen, Inc.
- [39] G. A. Riveros, Burgos, J. (2009). "Numerical Investigation of Miter Gates," *US Army Corps of Engineers, Information Technology Laboratory*, ERDC/ITL TR-09-1.
- [40] J. Marin (1962). "Mechanical Behavior of Engineering Materials," *Prentice Hall*, Englewood Cliffs, NJ.
- [41] J. E. Shigley, and Mischke, C.R. (1989). "Mechanical Engineering Design," *McGraw-Hill*, New York, New York.
- [42] Eurocode_3 (1993). "Design of steel structures - Part 1-9: Fatigue," *European Standard EN 1993-1-9*, European Committee for Standardization, Brussels, Belgium.
- [43] W. D. Pilket (2005). "Formulas for Stress, Strain, and Structural Matrices, 2nd Edition," *John Wiley and Sons, Inc*, Hoboken, NJ.

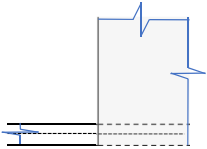
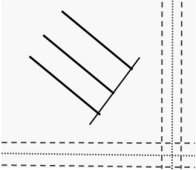
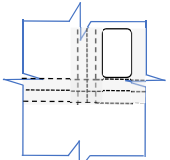
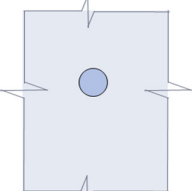
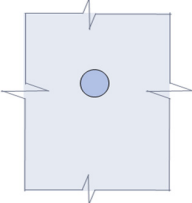
A1. Identification of Critical Sections

Table 11: List of identified critical sections, detail diagram, AASHTO category, and damage

Section	Sketch	Type	Category	Damage (N/N _r)
Section F1		1.5	D	No Damage
Section F2		7.1	E	No Damage
Section F3		71	E	No Damage
Section F3		7.1	E	No Damage
Section F4		7.1	E	No Damage
Section F5		6.1	E	No Damage

Section F6		7.1	E	No Damage
Section F6		7.1	E	No Damage
Section F7		6.1	E	1.91032E-07
Section F8		6.1	E	No Damage
Section F9		6.1	E	3.24412E-07
Section F10		6.1	E	1.06787E-05
Section F11		6.1	E	1.03828E-05
Section F12		7.1	E	9.1412E-06

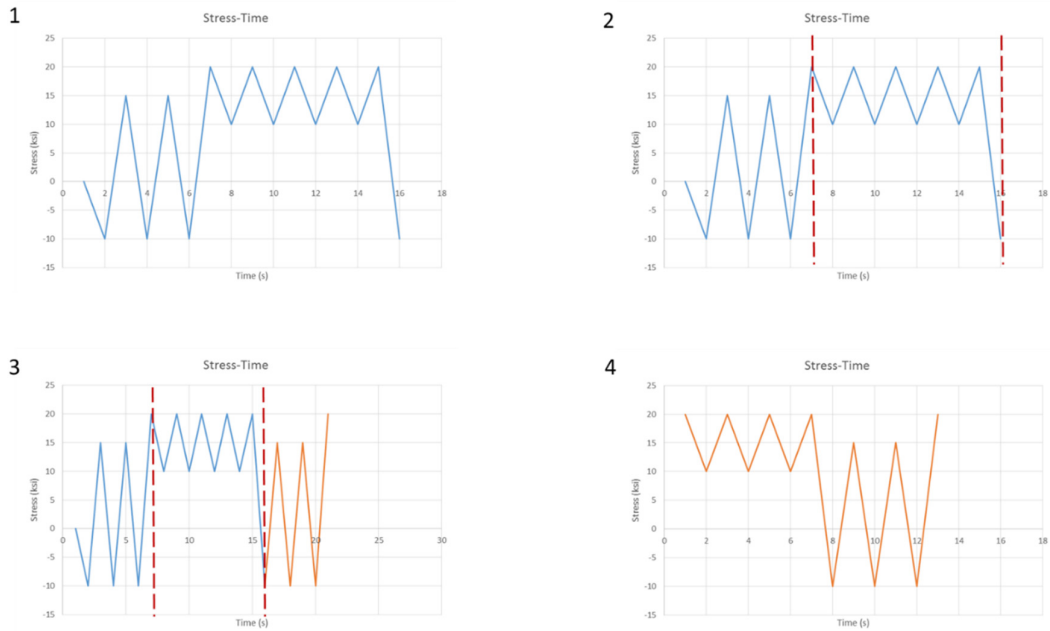
Section F13		6.1	E	1.17139E-05
Section F14		6.1	E	1.15013E-05
Section F15		7.1	E	9.70907E-06
Section F16		7.1	E	8.57359E-07
Section F17		7.1	E	8.57359E-07
Section F18		5.3	C	No Damage
Section F19		7.1	E	No Damage
Section F20		6.1	E	1.02327E-05
Section F21		6.1	E	9.56954E-06

Section F22		7.1	E	7.11418E-06
Section F23		5.3	C	No Damage
Section F24		7.1	E	1.37003E-06
Section Inside Hole 1		1.5	D	8.95048E-07
Section Inside Hole 2		1.5	D	5.0689E-07

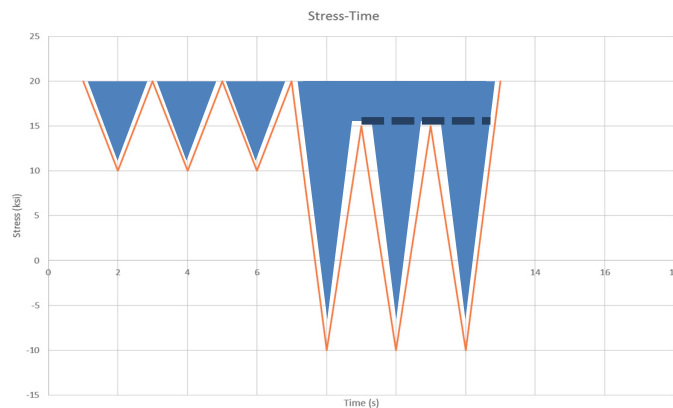
A2. Reservoir Cycle Counting Procedure

Cycle counting is used to get data from stress-time graph for fatigue analysis. There are two methods for cycle counting: reservoir cycle counting and rain flow cycle counting. The reservoir counting method was chosen because it was a better fit for the stress-time graphs from the output data.

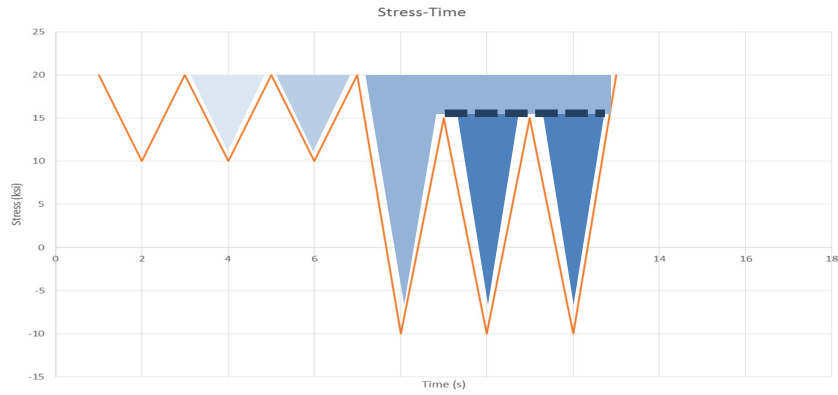
1. Shift part of the cycles so that the highest peaks are the starting point and ending point.



2. Imagine that the new graph is a reservoir filled with water.



3. Drain the reservoirs from the bottom of each valley.
 - a. Note the stress range from each drainage
 - b. Note the number of cycles per drainage. (Each valley is a cycle)



4. Create a table with the number of cycles at each stress range.

No. Cycles	Stress Range [ksi]
3	10
1	30
2	20

A3. Goodman S_e Calculations

This section describes how to calculate the fatigue endurance limit (S_e) using the Marin Equation. The 5th edition of *Mechanical Engineering Design* describes the process used to acquire the fatigue endurance limit [41]. The Marin equation is shown here as Equation 12.

$$S_e = k_a k_b k_c k_d k_f S'_e \quad \text{Equation 12}$$

The endurance limit, S'_e , is based on results from a rotating beam specimen, and is calculated using Equation 13.

$$S'_e = \begin{cases} 0.5 * S_{ult} & S_{ult} \leq 200 \text{ ksi} \\ 100 \text{ ksi} & S_{ult} > 200 \text{ ksi} \end{cases} \quad \text{Equation 13}$$

Modification Factors

Surface factor k_a

Cracks often initiate at the surface of the material. The surface modification factor assesses the quality of the finished surface along with the tensile strength of the material. Equation 14 calculates the factor k_a .

$$k_a = a S_{ult}^b \quad \text{Equation 14}$$

Table 12 determines the coefficients a and b . The component is hot-rolled with corresponding values for the coefficients determined from Table 12, and an ultimate strength of $S_{ut} = 65 \text{ ksi}$ for A572 steel. The surface factor is $k_a = 0.7189$.

Table 12. Parameters for Marin surface modification factor

Surface Finish	Factor a, S_{ut} given in ksi	Exponent b
New Ground	1.43	-0.085
Machined or cold-drawn	2.7	-0.265
Hot-rolled	14.4	-0.718
As-forged	39.9	-0.995

Size factor k_b

The size factor is based on volume. The size factor for the rotating bar specimen is determined by fitting a curve to experimental results. Volume affects the probability of failure as the probability of stress interaction with a critical flaw increases as the volume increases decreasing the endurance limit. Equation 15 calculates k_b for members that are subjected to bending and torsion.

$$k_b = \begin{cases} 0.879d^{-0.107} & 0.11 \leq d \leq 2 \text{ in} \\ 0.91d^{-0.157} & 2 < d \leq 10 \text{ in} \end{cases} \quad \text{Equation 15}$$

There is no size effect for axial loading, therefore $k_b = 1$. An effective diameter, d_e is used in place of d , in Equation 4, when the member is non-circular. The effective diameter d_e is calculated in Equation 16.

$$d_e = 0.808\sqrt{bh} \quad \text{Equation 16}$$

The variable b is the base and h is the height of the member's cross-section. Equations for other cross-sections are given in [41].

The component is under bending and has a rectangular cross-section. The variables $b = 10 \text{ in}$ and $h = \frac{3}{4} \text{ in}$, therefore the effective diameter is $d_e = 2.21 \text{ in}^2$. The size factor is $k_b = 0.803$.

Load factor k_c

The way a component is loaded affects its fatigue strength. The load factor k_c considers axial, bending, or torsional loading, see Equation 17. Estimated values for k_c are given below. The component experiences bending therefore $k_c = 1.0$.

$$k_c = \begin{cases} 1.0 & \text{Bending} \\ 0.85 & \text{Axial} \\ 0.59 & \text{Torsion} \end{cases} \quad \text{Equation 17}$$

Temperature factor k_d

Surface temperature affects the endurance limit of the component because the ultimate strength, S_{ut} , varies with temperature. Higher temperatures cause the yield strength to decrease leading to ductile failure. Lower temperatures can cause a brittle failure. Equation 18 calculates the temperature factor.

$$k_d = 0.975 + 0.432(10^{-3})T_f - 0.115(10^{-5})T_f^2 + 0.104(10^{-8})T_f^3 - 0.595(10^{-12})T_f^4 \quad \text{Equation 18}$$

The temperature variable, T_f , is in Fahrenheit and within the range $70 \leq T_f \leq 1000$ °F. The temperature factor, at the average water temperature $T_f = 75^\circ\text{F}$, is $k_d = 1.001$.

Reliability factor k_e

As the percent of reliability increases the reliability factor k_e decreases. Fatigue is based on the number of cycles a component is subjected to and the S-N curves used to determine fatigue endurance limits are based on statistical data. Figure 61 shows the uncertainty of the S-N curve data leads to a mean strength value within a standard deviation in a normal distribution plot. Reliability is the degree that a measurement, data, or calculation can be trusted. As reliability increases the component failure area, illustrated in Figure 61, decreases and along with the reliability factor. Table 13 gives percentages of reliability with the corresponding reliability factor, k_e . A conservative estimate of 50% reliability was chosen for section 13, and the reliability factor is, $k_e = 1.0$.

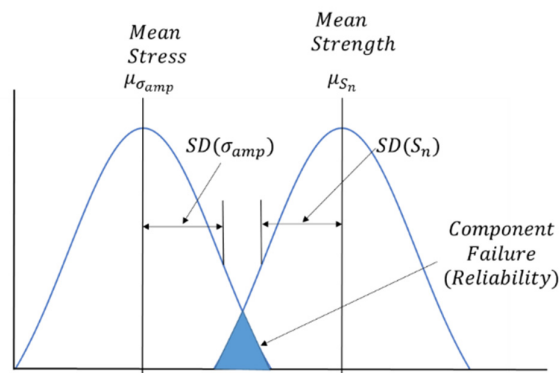


Figure 61. Mean stress and strength curves

Table 13: Reliability factors corresponding to 8% standard deviation of the endurance limit

Reliability, %	Reliability Factor, k_e
50	1.000
90	0.897
95	0.868
99	0.814
99.9	0.753
99.99	0.702
99.999	0.659
99.9999	0.620

Miscellaneous-Effects factor k_f

The miscellaneous-effects factor takes into consideration other environmental factors that can affect the fatigue endurance limit. Miscellaneous-effects factor considers influences such as corrosion, electrolytic plating, metal spraying, cyclic frequency, and frottage corrosion. Since these values are environmentally dependent and hard to determine the miscellaneous-effects factor is assumed to be $k_f = 1.0$.

Calculating S_e

The endurance limit, S_e , is calculated for section 13. Assumptions were made about the type of steel, temperature, reliability percentage, and other environmental factors to determine the different factors. The cross-sectional area of section 13 was calculated to determine the size factor. Section 13 is in bending and therefore the load factor coefficient chosen corresponds with bending. Table 14 summarizes the different factors.

Table 14: Calculated Marin modification factors summary and modified endurance limit

Factor	Value
k_a	0.719
k_b	0.803
k_c	1.000
k_d	0.999
k_e	1.000
k_f	1.000
S'_e	32.500 ksi

The calculated endurance limit, using Equation 19, is $S_e = 18.8 \text{ ksi}$.

$$S_e = k_a k_b k_c k_d k_f S'_e. \quad \text{Equation 19}$$

A4. Friction Test Derivation

The coefficient of static friction between rusted steel and stainless steel is determined through an experiment. The rusted steel is used as a ramp that the stainless-steel block slides down. The test consists of raising the ramp until the stainless piece begins to move. Once the stainless-steel block begins to move the gravity force on the block overcomes the friction force, see Figure 62(b). Figure 62 demonstrates how the ramp experiment allows for the static coefficient of friction to be calculated.

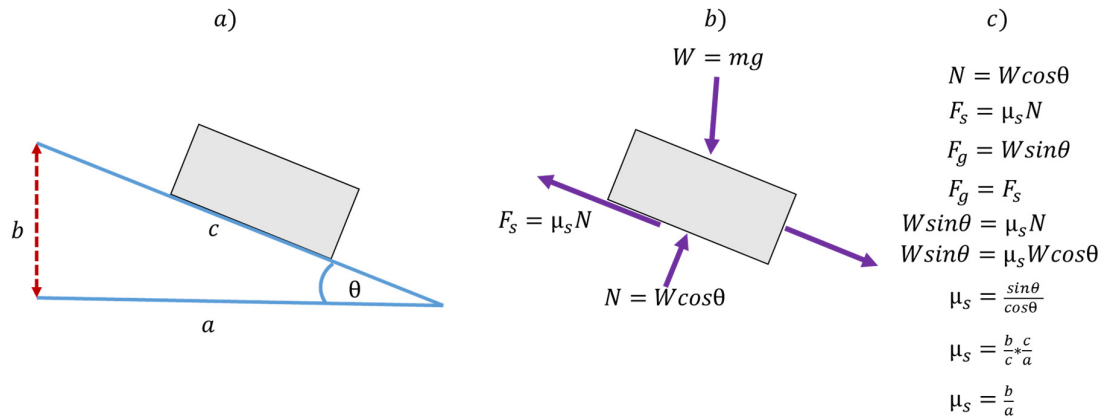


Figure 62. Static coefficient of friction test and derivation

A5. Friction Clamp Calculations

The friction force is calculated using a free body diagram (Figure 63), a known static coefficient of friction (μ), and a known pre-stress force (F_{pre}). There are two planes of friction, as seen in Figure 63. The two planes of friction divide the required clamping force (N) in half. The static coefficient of friction derived in Section A4 is $\mu = 0.34$. The derived pre-stress force is $F_{pre} = 366.57 \text{ kips}$. The calculated downward force is $N = 540 \text{ kips}$, see Figure 63.

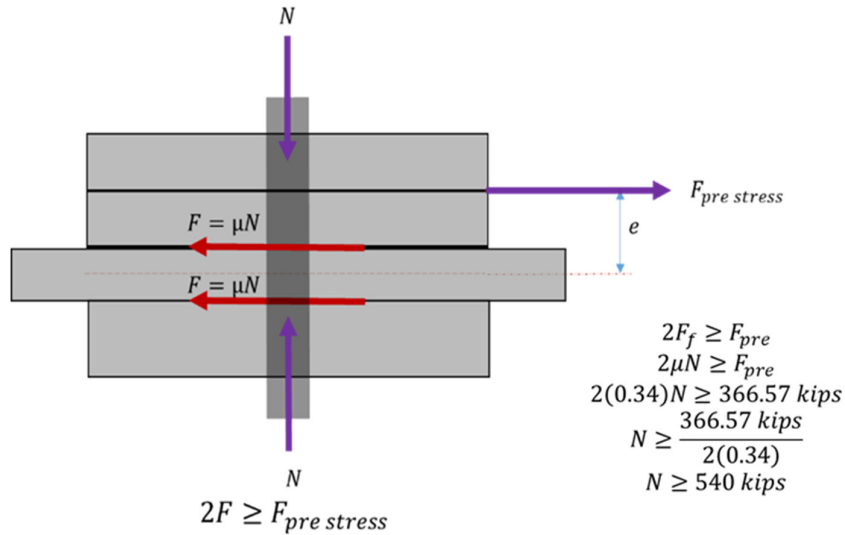


Figure 63. Free body diagram of friction clamp and derivation

A6. Cycle Estimation for Experimental Test

The estimated number of cycles to reach damage is determined using AASHTO Chapter 6. Table 6.6.1.2.3-1 from AASHTO Chapter 6 gives the category, constant (A) (ksi^3), and threshold (ΔF_{TH}) (ksi). The stress range (ΔF_N) is determined from the gate model max-in-plane stress data. Equation 20, from AASHTO Chapter 6 equation 6.6.1.2.5-2, is used to calculate the number of cycles to damage at the given stress range.

$$N = \frac{A}{\Delta F_N^3} \quad \text{Equation 20}$$

At the stress range $\Delta F = 24.467 \text{ ksi}$, calculated from the gate model, the number of cycles is $N = 73,468$. Due to the capability of the hydraulic actuator the tensile force applied during testing is 50 kips. The area the load is applied to is $A_{area} = 12.5 \text{ in}^2$. At the tensile load of $P = 50 \text{ kips}$ and $A_{area} = 12.5 \text{ in}^2$ the stress $\Delta F = 4 \text{ ksi}$. The number of cycles to damage at $\Delta F = 4 \text{ ksi}$ is $N = 17.2 * 10^6$.